PROJECT

Free-surface turbulence

Technical Report

Grid generated free-surface turbulence laboratory data

Mara Tonelli[*], Sandro Longo[**], Luca Chiapponi[**], Christian Mans[***], Miguel A. Losada[***]

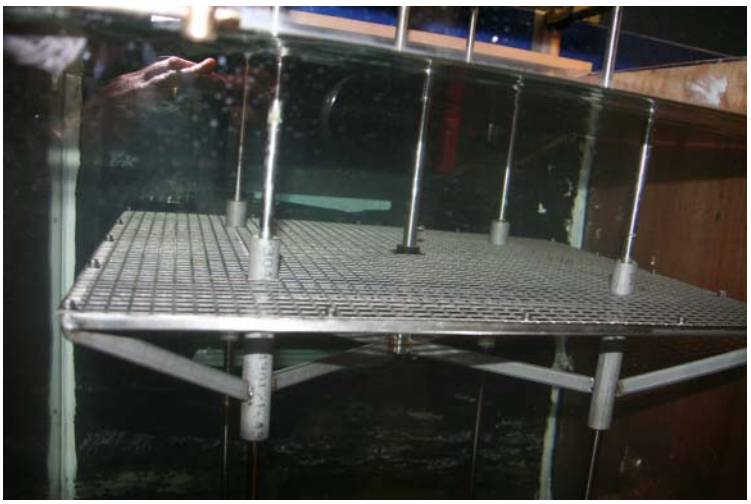

***Dipartimento di Georisorse e Territorio**

Università degli Studi di Udine, Italy

****Dipartimento di Ingegneria Civile**

Università degli Studi di Parma, Italy

*****Centro Andaluz de Medio Ambiente**

Universidad de Granada – Junta de Andalucía, Spain

April, 2010

Contents

List of figures and tables

1. Introduction

An understanding of the structure and dynamics of free-surface turbulence is essential for the correct interpretation of many interface phenomena, and the need for measuring the characteristics of turbulence beneath a free surface arises from its role in many important phenomena that take place at interfaces. These include gas and heat exchanges in the ocean, which have huge influences on the balance of chemicals and energy. In many engineering and industrial problems, most of the exchange takes place at the interface between a gas and a fluid, and many large-scale physical problems are governed by the characteristics of turbulence beneath an interface.

For this reason a series of tests were planned and carried out using an active grid to generate turbulence in water beneath an otherwise stationary interface air-water.

2. Free surface turbulence

The free surface represents a boundary for the flow domain and imposes some conditions: the material derivative of the free surface must be zero, while the tangential stresses should be zero (unless a shear is exerted by the overflowing gas). The interaction between turbulence and a free surface is expected to vary with the level of turbulence. The two main measures for describing the phenomenon are the Reynolds number and the Froude number, which generally increase together. At reduced Froude numbers, a free surface is essentially unaffected by the turbulence of the flow beneath it, is almost flat and imposes a reduction in only the normal velocity component. In this way, it can be described as a slip-free, rigid, flat surface. At higher Froude numbers, the free surface is not flat, and an energy exchange with the fluid flow ensues. Such an exchange is assumed to be initially very limited, but it becomes quite strong when a free surface loses its connectivity and contains air bubbles and drops. A great variety of free surface patterns and energy transfer mechanisms exist at the free surface, including capillary and gravity waves. A general description of the various levels of interaction between free surfaces and turbulence is reported in Brocchini and Peregrine (2001a). The authors describe the wide range of free-surface deformations that occur when there is turbulence at the surface, giving specific attention to turbulence in the liquid medium. Their discussion considers the effects of gravity and surface tension on the action of kinetic turbulent energy, where the authors heuristically outline a two-parameter description of surface behaviour in terms of length scale and turbulent kinetic energy.

Several experimental results are reported in the literature, often obtained using sophisticated techniques that are necessary to describe the complexity of the flow field. Komori et al. (1989) used Laser Doppler Anemometry to measure fluid velocity, an infrared scanner to measure free surface temperature, and a cold film probe to measure the temperature in the flow field. Most of the techniques adopted are image-based. An important experimental approach is the use of shadography (Settles 2001), which generates images that result from the refraction of light. Additionally, Particle Image Velocimetry (PIV) has been used to evaluate the interaction between a free surface and the flow beneath (Weingand 1996). Laser

scanning, with an output signal that is dependent upon the surface gradient, when used in conjunction with a laser-Doppler anemometer and a PIV, seems to be useful for detecting the space-time characteristics of the flow (Savelsberg et al. 2006). Dabiri and Gharib (2001) combined Digital Image Particle Velocimetry and a reflective mode of the Free Surface Gradient Detector method to evaluate the correlations between near-surface deformation and near surface velocity and vorticity. Their device was able to measure elevation in the range of ~1.2 mm. Quiao and Duncan (2001) used PIV to study gentle spilling breakers and to detail the flow field in the pre-breaking and breaking conditions. Savelsberg et al. (2006) measured the gradient field along the line of a turbulent free surface using a laser scanning technique coupled with laser-Doppler anemometry and Particle Image Velocimetry. In this way, they were able to measure 2D velocity fields beneath the free surface. In the field, radar instruments in ships, satellites, buoys or pressure sensors gives information on the free surface elevation, but this information yields limited information about the mean flow field and turbulence.

More detailed information is obtained using Direct Numerical Simulations (DNS), which are useful for the examination of low Froude number, free surface turbulence (Shen et al. 1999). This method also allows for the evaluation of pressure correlations, although this is beyond present experimental capabilities. In these simulations, the free surface is essentially flat, and no interactions are detected except by their effects on the turbulence of a boundary layer (a region adjacent to the free surface). The authors also distinguish a viscous surface layer and a blockage layer: in the viscous surface layer, which has a thickness scaling with the square root of the local Reynolds number, large Reynolds numbers yield fast changes in the vorticity from the external value to its value at the free surface. In particular, at low Froude numbers, the vorticity at the free surface has only a vertical component. In the blockage layer, there is a redistribution of the turbulent intensity, with a reduction in vertical velocity fluctuations and an increase in horizontal velocity fluctuations. The blockage layer is thick on the macro scale. This is not the only definition of the surface layer. Brocchini and Peregrine (2001b) describe the surface layer as the region occupied by two different phases, air and water; this definition can be used

only if the free surface is disconnected, having either bubbles in water or droplets in air.

Some other sophisticated models of large-eddy simulation also show new and characteristic behaviours of turbulence flux near the interface (Shen and Yue 2001). Hong and Walker (2000) developed a set of Reynolds-averaged governing equations for turbulent free-surface flow, with additional terms respect to standard Reynolds-averaged equations representing the effects of the boundary conditions. They also detail on the origin of the surface current, as observed in many fluid flows interacting with the free surface, analysing the different role of Reynolds-stress anisotropy and free-surface fluctuations.

In most (if not all) experiments and analyses, attention is focused on weak turbulence, with consequent weak and almost undetectable free surface fluctuations. This is indicated by the fact that papers on this topic do not describe the statistics of the free surface.

The importance of the analysis of turbulence in many environmental and industrial flows relies on the high efficiency of turbulence exchange (of momentum, thermal energy, chemical components) respect to molecular diffusion exchange. The early model of mass transfer at the interface were based on the role of the surface film. Higbie (1935) introduced a 'penetration' model to evaluate the parameters of the transfer processes near the free surface, assumed as a diffusion process. Danckwerts (1951) removed the conventional picture of a mass transfer between fluid and gas controlled by the liquid film; instead, a surface-renewal mechanism, controlled by turbulence, was postulated as the most important responsible of the process, affecting the exchange coefficients as used in the mass transfer equations of chemicals.

After conceptual models, the necessity to correlate the coefficients of the transfer equation to some measurable characteristic of the flow field near the interface was soon evident. A first theoretical analysis by Sirkar and Hanratty (1970), devoted to turbulent exchange near a wall, was later extended by McCready et al. (1986) to a slip-free interface in a cocurrent current air-water flow, with the aim of finding a relation between the transfer coefficients at the interface and the spectrum of the gradient of vertical velocity fluctuations. With a similar aim Tamburrino and

Gulliver (2002) fitted a linear model with experimental data obtained at the free surface in a moving bed flume.

Clearly turbulence is considered a major factor affecting interfacial phenomena. The classical analysis of turbulence is usually integrated by the description of turbulent fields in terms of their coherent structure. The coherent structures are interesting as they play a major role in transport phenomena in the flow field and at an interface. Due to the presence of bursting phenomena, surface-renewal motions in the interfacial region below a gas (air)-liquid (water) interface take place.

Komori et al. (1989), using flume experiments, demonstrated that the frequency of surface renewal is determined by the outer-flow variables and the Reynolds number, with mass transfer across the interface dominated by large-scale eddies and a mass transport coefficient proportional to the square root of the surface-renewal frequency. In almost all physical situations, coherent structures (such as eddies impinging the free surface) generate waves. The generation of waves upon the water surface and the interaction with the fluid turbulence have been analysed by Teixeira and Belcher (2006), who followed the by Phillips (1957). Phillips suggested a resonance of the turbulent pressure fluctuations in the air with the interface, resulting in the generation of waves. Among these waves, those matching the velocity of advection of the pressure fluctuations with their phase speed grew most rapidly. Teixeira and Belcher (2006) claim that pressure fluctuations in the water phase can also generate free surface waves, and that these can be much more energetic than waves generated by pressure fluctuations in the air. Phillips' theory has received only partial validation, as it requires measurements of the pressure field, and this is beyond present capabilities.

The experimental study of the interaction between turbulence and free surfaces has taken advantage of several "turbulent generators", which are described briefly herein.

The most common experimental apparatus is a constant-depth, two-dimensional open channel, with turbulence generated near the bottom and largely invariant in the streamwise direction, at least far from the inlet and outlet. Starting from the inlet of the channel, a boundary layer develops and then occupies the entire flow domain, up to the free surface. Bursting at the bottom favours eddy movement that can reach the

free surface and provide most of the 'renewal' of the surface (Nakagawa and Nezu 1977; Komori et al. 1989). The free surface suppresses vertical fluctuations and enhances tangential fluctuations, and, at small Froude numbers, the surface tension can be strong enough to prevent surface waves.

A moving-bed flume (a flume with a belt as a moving bottom) has been used to study the structure of the outer flow region and of the large streamwise vortices creating upwelling and downwelling motions at the free surface (Tamburrino and Gulliver, 1999).

Grid-stirred tank experiments with a free surface (Brumley and Jirka, 1987) have many attributes of channel flows in that the source of turbulence can be far from the free surface (to avoid coupling between the grid generation mechanism and the free surface response). They have the advantage that the turbulence field is homogeneous and isotropic in the horizontal plane, and nearly isotropic in the vertical plane.

Towed hydrofoils submerged near the free surface in an open channel have been used to distort the free surface and induce the breaking of the interface (Battjes and Sakai 1981). The hydrofoils generate a self-preserving turbulent wake flow that can be controlled, where the generated turbulence has a maximum near the toe of the breaking surface, before decaying downward and downstream.

The analysis of experimental instantaneous fluid levels and three-component fluid velocity measurements in a stationary flow field generated by a Crump weir in a laboratory flume using an ultrasonic distance sensor and a three-probe arrangement of an Ultrasonic Doppler Velocity Profiler (UVP) was carried out by Longo (2010a,b).

3. Laser Doppler Velocimetry

Laser Doppler Velocimetry (LDV) or Laser Doppler Anemometry (LDA) is a technique used to measure the velocity of fluids or, more precisely, of small particles advected in fluids. It is a non-intrusive, single point, optical technique which can be applied to perform up to three-dimensional velocity measurements.

Since the pioneering work by Yeh and Cummins (1964), LDV has attracted many researchers from various science fields and from the industry for its power, reliability and versatility, becoming quite popular. In fluid mechanics, it has proved particularly suitable for measuring flow velocities in complex or turbulent conditions (e.g. George and Lumley, 1973; Driver and Seegmiller, 1985; Adrian and Yao, 1986; Nezu and Rodi, 1986; Komori et al., 1989; Walker et al., 1995; Orlins and Gulliver, 2003).

The use of LDV systems offers high sampling rates and a good spatial resolution; it can reach a large part of the flow region, measuring near solid and free surfaces. It has a large dynamic range, not matched by other sensors. It is also able to provide information on the mean velocity, Reynolds stresses and higher-order statistical moments with a high degree of accuracy. On the other end, LDV is a single point measurement technique, hence, it does not give any information on the spatial structure of the flow; also, its application is non-trivial.

3.1. The principle of LDV

The functioning principle of LDV is relatively simple: it consists of determining the velocity of a fluid by measuring the Doppler shift of the laser light scattered by small, naturally buoyant particles carried within the flow.

The technique exploits the coherent nature of the laser light by which an interference pattern is produced at the crossing of two laser beams having the same wavelength. Such interference, or fringe, pattern consists of equally spaced planes of alternated high (constructive) and low (destructive) light intensity (Figure 3.1).

When a particle passes through the fringe pattern, it scatters the laser light and the intensity of the reflected light varies with the intensity of the fringes. The light scattered by the particle is collected by a photodetector, which transforms the optical

signal into an electrical signal; the signal produced by a single particle passing through the beam crossing is called a burst.

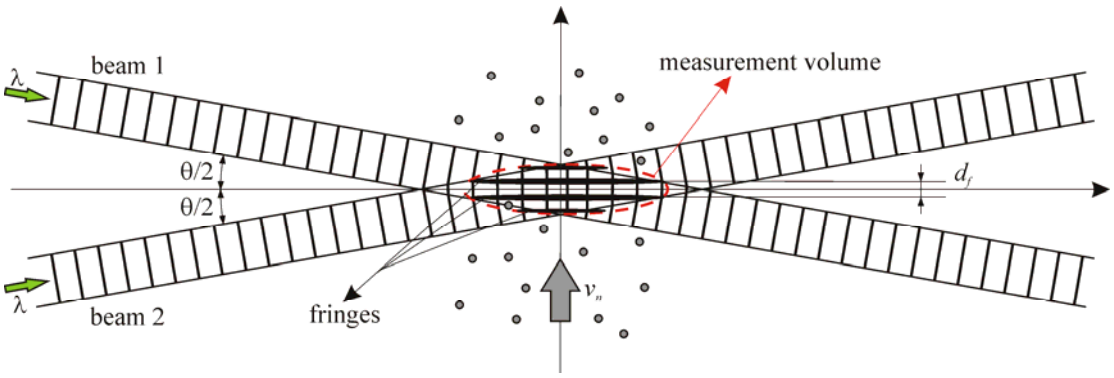

Figure 3.1. Sketch of the beam configuration and of the generated fringe pattern

Figure 3.2 shows an ideal burst signal (a real burst signal would have noise superimposed on it): the amplitude of the signal is proportional to the intensity of the scattered light. As can be seen, there exists a long modulation due to the structure of the laser light, which has a spatial Gaussian intensity distribution, and a short fluctuation due to the alternation of high and low intensity layers in the fringe pattern.

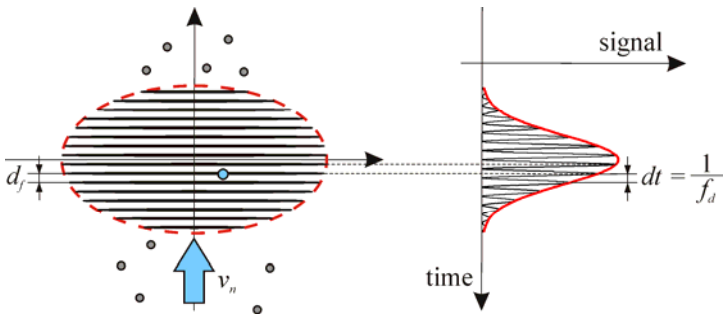

Figure 3.2. Sketch of the measurement volume horizontal plane section and example of a ideal burst signal generated by a particle crossing the measurement volume

The time scale of the short fluctuation coincides with the time it takes a particle to cover the distance between two adjacent fringes. In fact, the frequency (f_d) of the burst signal is related to the particle velocity through the relation:

$$v_n = d_f \cdot f_d \tag{3.1}$$

where v_n is the component of the particle velocity perpendicular to the bisector of the two beams and d_f is the distance between the fringes (Figure 3.1).

The spacing of the fringes is characteristic of the system; depending solely on the wavelength of the laser light (λ) and on the angle (θ) between the two incident beams (Figure 3.1):

$$d_f = \frac{\lambda}{2\sin(\theta/2)} \tag{3.2}$$

Hence, the burst frequency merely depends on the particle velocity as

$$f_d = \frac{2\sin(\theta/2)}{\lambda} \cdot v_n \tag{3.3}$$

Equation (3.3) only gives a relationship between the burst frequency and the magnitude of the particle velocity but it does not bear any reference to the direction of such velocity. In fact, in the described conditions, particles moving with the same velocity in opposite directions generate exactly the same burst signal and are therefore undistinguishable.

In order to correct this ambiguity and determine the direction of the flow, the frequency of one of the beams is shifted by a known amount f_s by a Bragg cell. This causes the fringe pattern to oscillate at the shift frequency f_s and, as a result, the fringes appear to translate from the shifted beam towards the unshifted beam at a velocity $v_s = d_f \cdot f_s$. With this configuration, a particle moving at a given velocity will generate bursts with different frequencies depending on whether it is moving in the same direction of the fringes or against them. This can be easily understood considering a reference system moving solidly with the fringe pattern at the velocity v_s and calculating the particle velocity in relative reference system for the two opposite conditions. It is found that the relative particle velocity v_n' is $v_n' = v_n + v_s$

when the particle is moving against the fringes, whereas it is $v_n' = v_n - v_s$ when the particle is moving in the same direction of the fringes. As a consequence, the frequency of the burst generated by a particle moving against the fringes will be higher than the one generated by a particle moving in the opposite direction.

The frequency of the burst generated by a particle crossing the measurement volume is:

$$f = f_s \pm f_d \tag{3.4}$$

where the plus sign holds for particles moving against the fringes and the minus sign for particles moving in the same direction of the fringes.

A different interpretation of the functioning principle of LDV consists of assuming that the particle crossing the measurement volume scatters the light of the two incident beams separately. Since the particle is moving, the scattered light is Doppler shifted (hence the name of the technique) and the frequency shift, which depends on the wavelength and direction of the beams, is different for the two laser beams. For instance, for the configuration represented in Figure 3.3:

$$f_{d1} = \frac{2v_n}{\lambda}\cos(\beta_1)\sin\left(\frac{\alpha_1}{2}\right) = \frac{2v_n}{\lambda}\cos\left(-\frac{\theta}{4}\right)\sin\left(-\frac{\theta}{4}\right) \tag{3.5}$$

$$f_{d2} = \frac{2v_n}{\lambda}\cos(\beta_2)\sin\left(\frac{\alpha_2}{2}\right) = \frac{2v_n}{\lambda}\cos\left(\frac{\theta}{4}\right)\sin\left(\frac{\theta}{4}\right) \tag{3.6}$$

As can be easily noted, the difference of the two frequency shifts is related to the particle velocity by the expression

$$f_d = \frac{f_{d1} - f_{d2}}{2} = \pm v_n \frac{2\sin(\theta/2)}{\lambda} \tag{3.7}$$

where, in a generic case, the sign depends on the direction of the velocity.

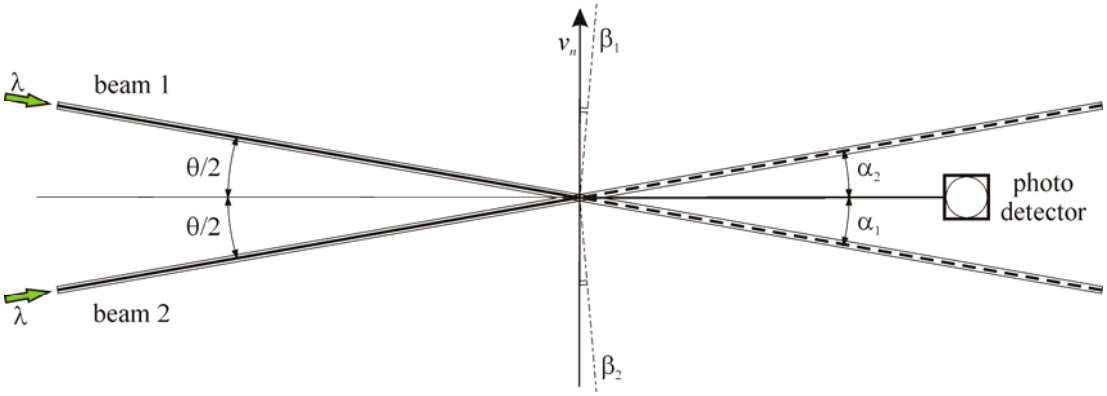

Figure 3.3. Sketch of the beam and photodetector configuration for the evaluation of the Doppler shift

When the scattered light from the two beams is collected at the front of the photodetector, heterodyne interference occurs on its surface. Because of the difference in frequency of the two scattered beams, the interference produces fluctuations, or beats, of the light intensity at a fixed point. There are two frequencies in a beat: a higher one, equal to one half of the sum of the frequencies of the two scattered beams and a lower one, equal to one half of their difference. This last signal coincides with the burst and it is the only one detected by the photodetector. Based on the previous remarks, the burst frequency is

$$f = \frac{(f_1 + f_{d1}) - (f_2 + f_{d2})}{2} = f_s \pm f_d \tag{3.8}$$

Once the scattered light is collected by the photodetector and transformed into an electric signal, this is processed to determine the frequency f_d. First, the Gaussian modulation of the burst signal (named pedestal) is removed by means of a high-pass filter; then, the evaluation of the burst frequency f_d can be performed in different ways: by counting the number of zero-crossings per unit time, by determining the peak frequency of the signal calculating its Fourier transform, or by using a correlation algorithm to compute the autocorrelation of the signal, which is maximum for lags that are multiples of the signal time period.

As anticipated, LDV is a single-point technique because the velocity is measured only when the particles pass through the crossing between two beams; therefore, the

measurement volume of a LDV system coincides with the beam crossing and it has the shape of an ellipsoid.

A single pair of incident beams measures a single velocity component, perpendicular to the bisector of the two incident beams. In order to measure two or three velocity components, a second and a third pair of laser beams must be added to the system. Each pair of beams must have a specific wave length so that the burst signals corresponding to different beam crossings can be distinguished by filtering. For multi-component measurements the three beam crossings should coincide, so that the velocity components are measured at the same point.

3.2. Bias and noise in LDV systems

A key feature of LDV measurements, which strongly impacts the analysis of the data, is their intermittent and random nature. Since the flow velocity is sampled only when a particle passes through the measurement volume and this is a random phenomenon, the distribution of the velocity data is not uniform in time. This randomness depends on the optical parameters of the system, the particle concentration and the flow velocity itself. Such a dependence is confirmed by the fact that a larger number of samples is generated when the velocity is higher as more particles cross the measurement volume per unit time. As a consequence, if the flow statistics are evaluated by means of the sample statistics of the measured particle realizations, a bias towards high velocity values is introduced – a problem was first recognized by Mc Laughlin and Tiederman (1973). The magnitude of the bias error depends on the magnitude of the velocity variations around the mean and becomes significant if the sampling rate is considerably larger than the frequency of the mean velocity fluctuations.

The velocity bias error can be eliminated in two different ways. The first way consists of weighting each individual measurement by a factor which is inversely proportional to the probability of sampling it. Different weighting functions, based on the transit time, the time lag between data points or the reciprocal velocity, can be used (e.g. Mc Laughlin and Tiederman, 1973; Hoesel and Rodi, 1977). The second method consists of reconstructing the original signal or, if the data rate is high enough, of sampling the data at constant, fixed time intervals (Edwards, 1987).

Another source of sampling non-uniformity is the shape of the measurement volume. The rate of measured data is proportional to the projection area of the measurement volume normal to the flow direction. Because of the prolate shape of the measurement volume, the area of the projection varies with the direction of the flow. Again, the sampling scheme depends on the velocity (Nobach, 1999).

The randomness of the measurements, together with the velocity bias, adds complexity to the spectral analysis of LDV data. A variety of techniques, like reconstruction or slotting techniques, has been introduced to obtain reliable spectral information from randomly distributed data (Benedict et al., 2000). For multi-dimensional systems, the randomness of the data also implies that the different velocity components may not be recorded at exactly the same times.

The random distribution in time of the velocity samples, by velocity bias and also by inhomogeneous distribution of tracer particles, can be viewed, together with errors in the individual velocity measurements, as noise added to the signal (Ramond and Millan, 2000).

There are several other sources of noise in the LDV signal:

- the light scattered from outside the measurement volume, dirt, scratched windows, ambient light, multiple particles;
- unwanted reflections from windows, lenses, mirrors;
- the occurrence of velocity gradients in the measurement volume;
- secondary electronic noise;
- the presence of errors in the optical system, higher order laser modes or optical noise;
- the temporal and amplitude resolution of the detector (see for instance, Durão et al., 1980) and
- the signal processing (e.g. finite time broadening).

LDV measurement systems usually produce signals with a lower signal-to-noise ratio than data from other measuring techniques, such as hot-wire anemometry(Ramond and Millan, 2000). This trend is enhanced when backward scatter configurations are used, i.e. when the receiving optics is integrated with the transmitting optics. In fact, even if the particles scatter light in all directions, the highest intensity of the reflected light will be on the forward side, that is on the

opposite side of the incident beams, with respect to the position of the measurement volume. Therefore, ideally, the best location for the deployment of the photodetector would be on the forward side (forward scatter); however, practically, this is not always convenient, because the photodetector must be positioned carefully to ensure a good view of the measurement volume while limiting reflection and this can be a lengthy procedure. A backward scatter configuration is easier to manage and operate, especially for multi-component systems, but is likely to receive less intense reflected light.

4. Experimental facilities

This section presents a description of the facilities used to perform the experiments on free-surface turbulence.

4.1. Wave flume

The wave flume located in the Laboratorio de Dinámica de Fluidos Ambientales of the CEAMA (Centro Andaluz de Medio Ambiente) in Granada is 23 m long, 1 m high and 0.65 m wide (Figure 4.1). It is built in steel and Plexiglas. At one end of the flume, a piston-type wave maker is installed, whereas at the opposite end a wooden beach with a dissipative parabolic profile is present and followed by a flat bottom section filled with gravel. The wavemaker is equipped with an AWACs system for the absorption of reflected waves.

The test cases presented in this report consider the interaction of turbulence with a flat free surface, therefore, the wavemaker is never activated. In order to control the development of circulation patterns in the water volume, a smaller tank is built inside the flume. Two Plexiglas walls are installed crosswise inside the flume, isolating a portion of the channel with a rectangular horizontal section of 0.66×0.65 m and a height of 1 m.

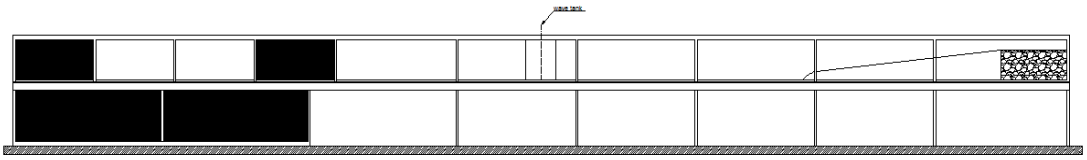

Figure 4.1. Wave flume

4.2. Grid

In the experiments, an active grid (Figure 4.2) is used to generate turbulence below the free surface. The grid has dimensions 554 × 554 mm and it consists of a 2 mm thick, perforated stainless steel plate. The holes are squares with a side of 10 mm and the distance between the centres of two adjacent holes (M) is 12 mm in both directions; the grid bars are squared and their side is 2 mm. The resulting solidity is 0.31 (i.e. the 31% of the plan area is covered by steel).

In the experiments, the grid is suspended horizontally inside the small tank built in the wave flume and moved along the vertical direction, stirring the water. The bearing of the grid consists of a stainless steel frame, on top of which an electrical motor is located and connected to a cylindrical vertical axle extending across the frame, which is the rod of a crank-connecting rod system operated by the motor itself. The axle is connected to the frame by a special joint which transmits axial compression and traction stresses but not shear stresses or axial torques.

Below the frame, the grid is centred on the vertical axle which transmits it a translational harmonic motion in the vertical direction; four slim legs, parallel to the axle and welded to the frame, constrain the motion of the grid to a vertical sliding, avoiding oscillation, torsion or tilting.

Adjustments in the motor speed and in the position of the crank pinning to the motor flywheel assembly allow the grid to move with frequencies between 0.3 and 3.3 Hz and peak to peak strokes varying in the range 30-150 mm.

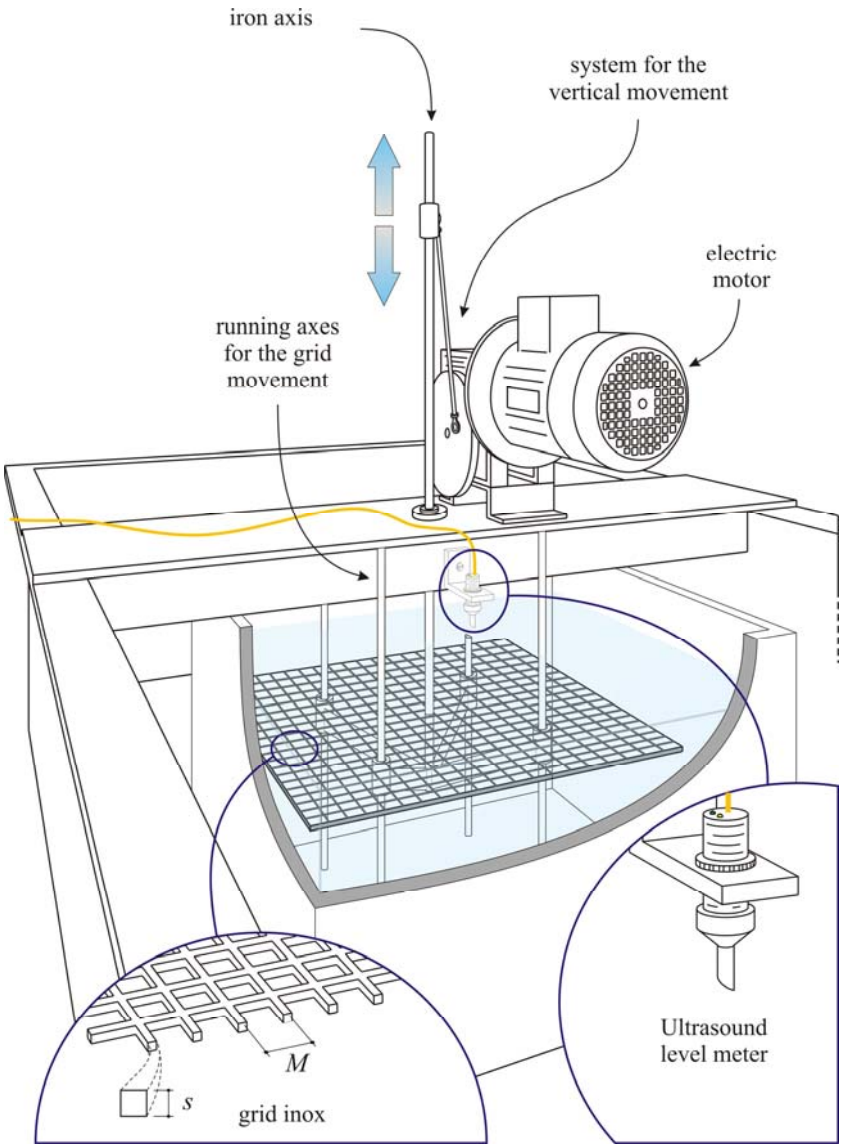

Figure 4.2. Experimental set-up

4.2.1. Grid position measuring device

The grid position is measured by a linear potentiometer ELAP PL2S. The instrument has a nominal stroke of 250 mm and it gives a strongly linear response (the linearity error is lower than 0.1%). The potentiometer is fixed to the grid system through two spherical joints, one constrained to the grid bearing and the other integral with the axle which transmits the vertical motion to the grid.

The potentiometer gives a voltage output signal in the range 0 – 10 V, through which it is possible to measure the amplitude and the frequency of the grid oscillations.

4.3. Water level gauges

Water level oscillations are measured by a ultrasonic water level sensor, model Q45UR, produced by the company Turck-Banner (Figure 4.3).

Figure 4.3. Ultrasonic water level gauge

The sensor consists of a piezoelectric transducer immersed in an alternate electrical field, whose voltage oscillates at a certain frequency; the transducer responds to the electric excitation, vibrating at a high frequency and emitting an ultrasonic pressure wave. The ultrasonic wave propagates in air towards the water free surface, where it is reflected. This reflected wave travels back to the sensor, where it is collected by the same membrane that emits the wave. The sensor measures the time elapsed between the emission of the ultrasonic pulse and the reception of the reflected waves and hence determines the distance (d) from the membrane to the target through the relation:

$$d = \frac{1}{2} c t_f \tag{4.1}$$

where t_f is the flight time of the ultrasonic wave and c is the celerity of the ultrasonic wave in air. Since c is a function of temperature, the sensor is equipped with a temperature gauge to compensate for the effects of temperature variations.

Some of the instrumental characteristics of the gauge are reported in Table 4.1. The emitted ultrasonic wave has a conical shape, with a diverging angle of 3.5 deg; therefore, the measurement is not precisely local and the averaging area, corresponding to the print of the ultrasonic cone on the water surface, varies with the distance between the emitting membrane and the target.

In this study, the instrument is set to give a voltage output signal, with a full range scale of 10 V. The gauge is calibrated to measure two possible ranges of distance: the whole nominal sensing range of the instrument, which corresponds to the distance window 50-250 mm, and a shorter range of distances (70-120 mm); the short range calibration provides an increased sensibility of the measurement when the free surface is close to the gauge. This last calibration is used in all the performed tests. The response time is 10 ms.

Table 4.1. Ultrasonic water level characteristics

Feature	*Range*
Supply voltage	15-24 V
No-load current	≤100 mA
Current analogue output	4-20 mA
Voltage analogue output	0-10 V
Load resistance	<500 Ω
Sensing range	50-250 mm
Resolution	0.1 mm
Switching frequency	3-100 Hz

4.3.1. Calibration of the level gauges

The voltage output of the ultrasonic sensor must be related to a metric water level signal. The input – output relation (mm – V) is determined by measuring a number of known distances; to do so, the water level is kept still and the gauge is moved to

known locations by means of a traverse system. For each location, the output signal is acquired for a time interval of 120 s, the mean voltage value is then computed and associated with the known distance from the water surface.

The long range calibration curve is plotted in Figure 4.4; the calibration output is linear.

The short range calibration curve is plotted in Figure 4.5; the calibration output is linear for the most part of the measuring range but it shows a distinct knee between 6.75 and 7 V. The conversion function from tension to distance values is therefore performed interpolating linearly between each couple of points mapped during the calibration procedure.

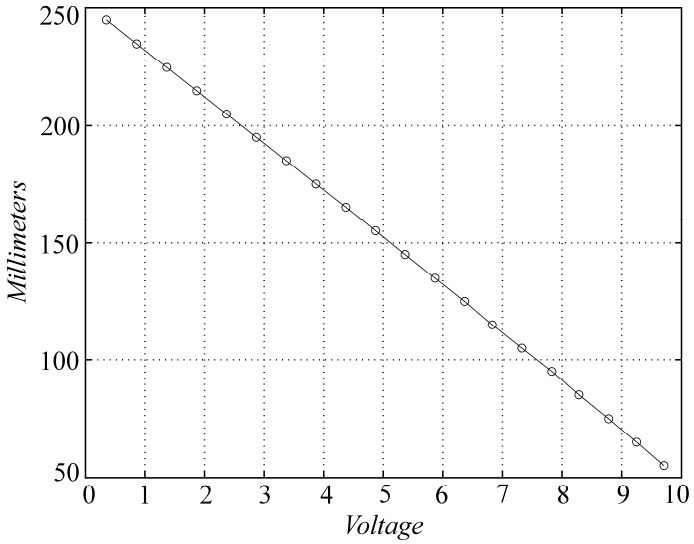

Figure 4.4. Ultrasonic water level gauge – long range calibration curve

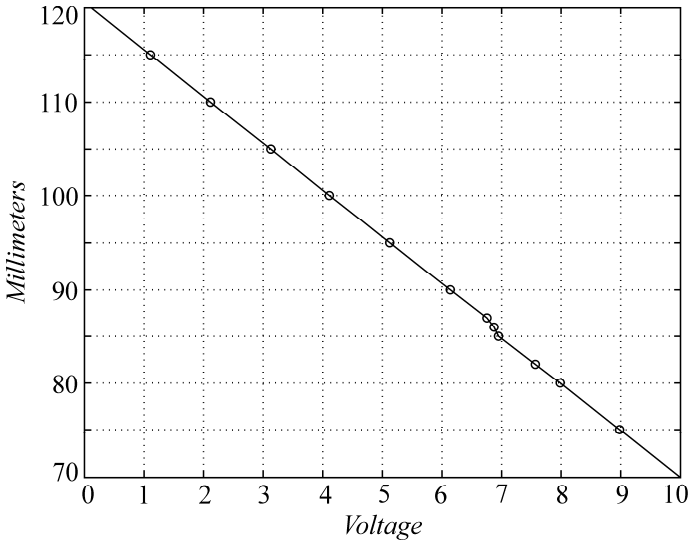

Figure 4.5. Ultrasonic water level gauge – short range calibration curve

The nominal resolution of the ultrasonic level sensor is 0.10 mm. Such a resolution is not restricted by the resolution of the 16 bit data acquisition card which uses 65536 points to represent a range of 20 V (from -10 V to 10 V) and therefore has a voltage resolution of:

$$\frac{20}{65536} \simeq 3.052 \cdot 10^{-4} \left(\frac{\mathrm{V}}{\mathrm{point}} \right) \tag{4.2}$$

For the short range calibration, the actual measuring range is 50 mm, thus the resolution can be expressed in terms of distance as

$$\frac{50}{10}\left(\frac{\mathrm{mm}}{\mathrm{V}} \right) \times 3.052 \cdot 10^{-4} \left(\frac{\mathrm{V}}{\mathrm{point}} \right) = 0.0015 \left(\frac{\mathrm{mm}}{\mathrm{point}} \right) \tag{4.3}$$

the resolution becomes 0.006 mm/point for the long range calibration.

Uncertainties in the ultrasonic distance measurements arise due to strong spatial gradients of the free surface, that generate lost echoes, and to gradients of temperature along the path of the sound that modify the celerity. The first source of uncertainty can be overcome by holding the last measured value in case of an absence of echo, with a negligible loss of information. The uncertainty due to

temperature gradients along the path of the sound can be quantified. Assuming a linear variation of the temperature between the emitter and the target, the relative uncertainty is equal to:

$$\frac{\Delta L}{L_0} = \frac{\Theta_1 - \Theta_0}{4\Theta_0} \tag{4.4}$$

where Θ_0 is the temperature near the emitter/receiver, L_0 is the distance to the target and Θ_1 is the temperature near the target. We have assumed a negligible uncertainty in the time of flight measurements. Assuming Θ_0 = 293 °K and $\Theta_1 = \Theta_0 \pm 1$ °K, the maximum uncertainty is equal to ± 0.2 mm. Another source of uncertainty is the non-stationary nature of the target. Considering that the echo is generated by a moving surface, a Doppler shift equal to $(2v_s/c)f_e$ may be expected, where v_s is the velocity of the surface, c is the celerity of ultrasound propagation in air and f_e is the frequency of the carrier. However, ultrasound waves are not dispersive in air, and the small frequency shift does not affect the computation of the distance of the target (hence, the instantaneous water level measurement). Finally, the level of electric noise is correspondent to an error in water level measurement of $\Delta\eta = \pm$ 0.1 mm.

Under our experimental conditions, the overall uncertainty in the free surface level measurements (including the non-linearity and repeatability of the instrument) is estimated to be ± 0.3 mm.

4.4. Laser Doppler Velocimeter

A two-component (2D) Laser Doppler Velocimetry system produced by TSI Inc. is used to measure the fluid velocity locally along two orthogonal directions. For this purpose, the system works with two pairs of laser beams having different wavelengths (λ_g and λ_b); each couple of beams defines a plane and the two planes are mutually normal.

The laser is an Innova 70 Series water cooled Ar-Ion laser, which can reach a maximum power of 5 Watts. The TSI optical modular system consists of a multicolour beam separator to divide the laser beam in two colour components

(green – λ_g = 514.5 nm and blue – λ_b = 488.0 nm) and then each component into two beams; a Bragg cell to introduce a frequency shift to one beam for each colour; four fibreoptics couplers to convey the beams towards the transmitting lens and a two-component fibreoptics transmitting/receiving probe. The probe provides the convergence of the laser beams into the measurement volume and, since the system works in backward scatter mode, it also collects the scattered light sending it to the elaboration system. The focus length of the probe lens is 363 mm, the beam spacing is 50 mm and the half-angle between the incident beams is 3.96°.

The measurement volume defined by the intersection of the four laser beams has the shape of a prolate ellipsoid whose dimensions are of the order 0.08×0.08×1.25 mm; the cross sections of the measurement volume on the two planes defined by each beam pair are ellipses and present an interference fringe pattern with a fringe spacing which depends on the wavelength of the light and the angle between the two incident light beams of the couple, the order of magnitude of the fringe distance is 3.5 μm.

The collected scattered light, carrying the Doppler frequency information, is sent by a transmitting fibre to the Photo Detector Module (PDM) which includes a series of photomultiplier tubes to identify and amplify the optical signal, a beam splitter and a high-pass filter. Inside the PDM, the signal is detected, amplified and it has the pedestal removed; the elaborated signal is then sent to the signal processor Flow Size Analyzer (FSA) which processes the analogue burst signals and sends the results (Doppler frequency, velocity, time stamp, transit time, channel number) to a computer.

Uncertainties in LDV systems are due to velocity bias, inhomogeneous distribution of tracer particles, errors in the individual velocity measurements, occurrence of velocity gradients in the measurement volume, the presence of errors in the optical system, the resolution of the detector and the signal processing. These may be viewed as noise adding up to the wide bandwidth electric noise from stray light (reflections or scattering of laser light from walls, windows or optical components), the photomultiplier and the associated electronics.

A weighting function based on the transit time is applied to correct the velocity bias due to the dependence of the sampling on the velocity magnitude.

It should be noted that, since the LDV system performs single-point velocity measurements, it is important to accurately separate turbulence from background large scale motions.

4.4.1. Laser set-up

This section outlines the procedures performed to increase the data rate – the number of particles crossing the measurement volume in a given time interval – and to improve the quality of the data.

Firstly, the convergence of the laser beams was checked. A good convergence of the beams is, in fact, the main requirement for the achievement of high-quality measurements and it implies three conditions:

- the two beams of each pair must intersect by at least the 80% of their diameter;
- the crossings of the two pairs must overlap by at least the 80% of their diameters;
- the crossing of the four beams must be aligned with the receiving fibre.

The first condition aims at achieving a minimum size of the measurement volume and, hence, a minimum number of fringes, which is important to obtain reliable velocity measurements. The second conditions requires that the two measurement volumes defined by the two pairs of beams coincide. The third condition assures that the measurement volume and the viewing volume, namely the zone from which light is most efficiently collected by the receiving fibre, are aligned, so that the maximum of the light scattered by particles crossing the measurement volume is acquired by the system.

Since the initial configuration of the laser system did not fulfil the crossing and alignment requirements, a delicate procedure of beam steering has been performed and it is described in Appendix B.

A second requirement, which should be satisfied to obtain good velocity measurements, is the balance of the beams power: the four beams should come out from the transmitting lens with sensibly equal intensity. In order to achieve this conditions, attention must be paid in the procedure of aligning the heads of the

transmitting fibres with the light beams emitted by the multi-beam separator. This procedure was performed daily, before starting to run the tests.

Finally, it turned out to be extremely important to run the tests in clear water, seeded only by suitably selected particles: the quality of the water and of the seeding particles strongly affects the quality of the measurements. At the beginning of each day of testing, the water in the tank was changed and replaced with fresh, clean water; upon which, particles were gradually added until the correct concentration of the tracer in water was reached. After several trials, TiO_2 particles were selected as an appropriate tracer.

It is well known that the system measures the velocity of the particles and not of the fluid; however for small light particles the motion of the particles is almost coincident with the fluid motion and a large volume of literature is available regarding the origin of uncertainties for this approximation.

5. Experiments

This section describes the experiments carried out to study grid generated free surface turbulence.

5.1. Experimental set-up

The series of test cases described in this report is performed in a small tank built inside the wave flume (Figure 5.1). The tank is 0.66 m long, 0.65 m wide, and 1 m high; it is bounded along the longitudinal direction by two Plexiglas walls, held in place by a wooden structure, and along the transverse direction by the side walls of the flume.

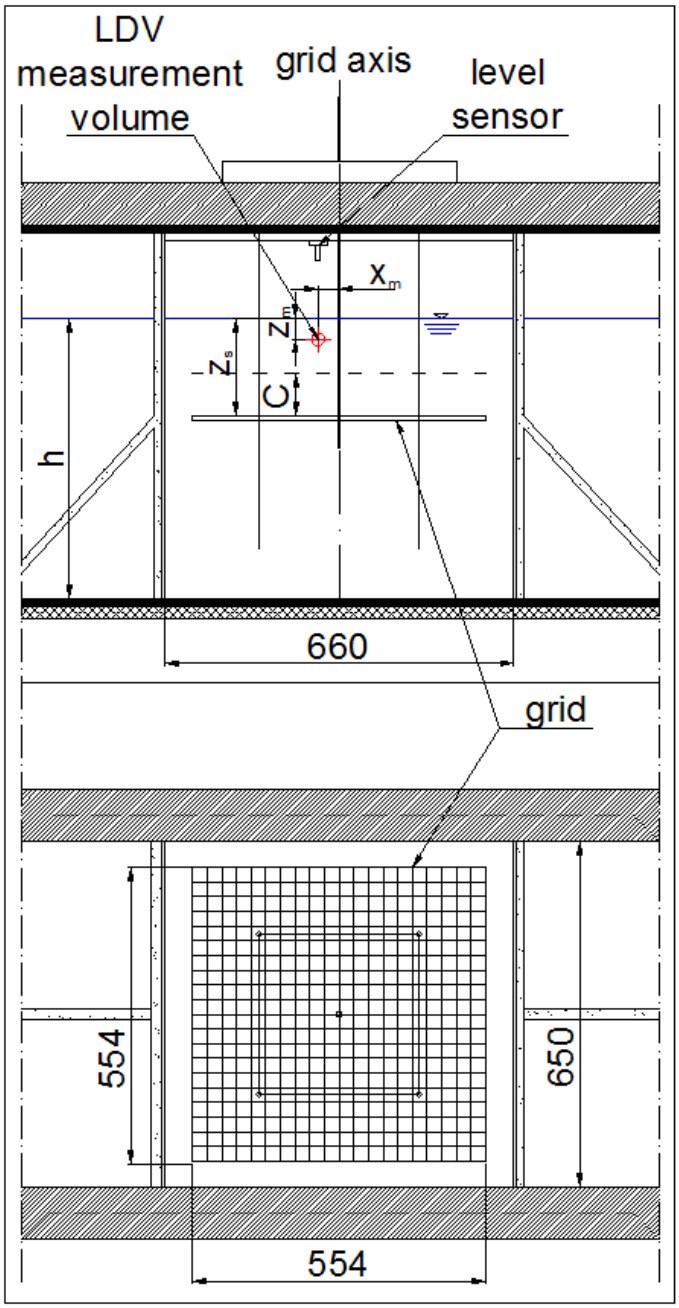

Figure 5.1. Sketch of the wave tank set-up (measures are expressed in mm)

The tank is filled up with clear water and the still water depth, i.e. the distance between the free surface and the bottom of the flume in still water conditions, is indicated by the symbol *h*.

The grid is suspended horizontally inside the small tank and moves along the vertical direction, aggravating the water. The distance between the free surface and the grid plate when the grid lies at the farthest point from the water table is indicated

by z_s; the stroke of the grid is indicated by C (Figure 5.1). The frequency of the grid oscillation is 3.3 Hz or 3.0 Hz in all test conditions.

The transmitting/receiving probe of the LDV is mounted on a traverse system and placed in front of the flume. The traverse system allows horizontal (parallel to the flume) and vertical displacements of the probe, which are prompted and controlled by means of a MatLab code. The reference system for the transverse displacements and, hence, for the velocity measurements, has its horizontal origin (x = 0) on the axis of the grid and its vertical origin (z = 0) at the still water level. The position of the still water level is located at the beginning of each series of measurements and the crossing of the LDV beams is aligned at the free surface.

In addition to the position of the probe, its inclination (Figure 5.2) with respect to the horizontal plane can also be changed. An angle of 0 deg favours a high data rate, as scattered light is intercepted more easily by the receiving optics, but positive angles enable velocity measurements closer to the free surface, as indicated in the figure.

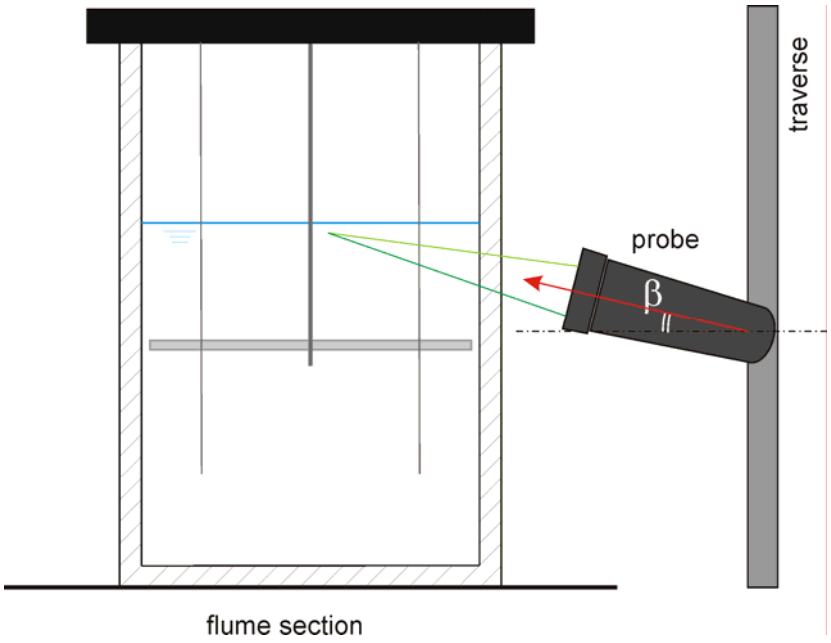

Figure 5.2. Set-up of the LDV probe

The last parameter set for the LDV velocity measurements is the orientation of the laser beams. The laser reference system can be rotated by an angle θ with respect to the external reference system made of the horizontal and vertical axes *x* and *z* (see Figure 5.3). For the purposes of the present experiments, it is useful to introduce a rotation θ = 45° in order to reach points closer to the free surface. It should be noted that the LDV reference system is the system from which the velocity components are actually measured

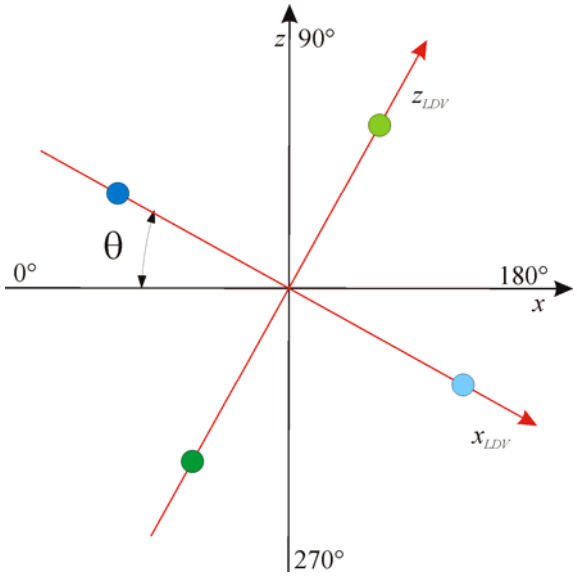

Figure 5.3. External (*x*-*y*) and LDV reference systems (θ is the probe angle).

The position of the free surface is measured by a ultrasonic water level sensor. As the experiments aim to relate the oscillations of the free surface to the characteristics of the turbulent flow underneath it, the sensor must be located precisely on the vertical axis of the LDV measurement volume. In order to align the ultrasonic water level sensor with the LDV measurement volume, a slim metal bar is hung beneath the membrane of the water level gauge and used as a target for the crossing of the laser beams.

The acquisition system consists of two personal computers, a National Instrument DAQ board equipped with 16 channels of analogue input, 2 channels of analogue output, 8 lines of digital I/O and a 12-bit AD converter.

Grid position data, measured by a linear potentiometer, and free surface elevation data, measured by the ultrasonic sensor, are acquired by the NI-DAQ board at 100 Hz and stored on a PC. The channels are used in differential mode, with an input range of ±10 V. The acquisition is started and managed by a suitably developed MatLab code *mks.m*. Collected data are visualized in real time and used to check the amplitude and frequency of the grid oscillation and the quality of the signal transmitted by the water level gauge. A first elaboration of the data is performed during acquisition: water level data are converted from volts to millimeters and filtered at an assigned cut-off frequency; both the row and processed data are saved in both *.mat* (MatLab) and *.out* (ASCII) files.

Velocity measurements are acquired by the LDV system and stored independently by a second PC; this acquisition is triggered to free surface elevation data in order to have a common time origin for the two series of data. Data acquisition from NI-DAQ (US level and grid position) sends a trigger signal to the laser signal processor (FSA3500) which sets the time stamp of the velocity measurements back to zero. On using the software *elaborazione_laser.m* the data from LDV are conditioned, eliminating the interval time before triggering signal and are saved in .mat files.

The frequency of acquisition of the velocity depends on the LDV set-up and on the flow conditions (see section 3) hence it can not be forced to a specific value.

5.2. Test cases

The series of tests performed during the experimental activity include some preliminary tests, conducted to evaluate the LDV performances and to verify the suitability of the measurements to compute the Reynolds stresses, and some final tests which investigate the structure of free surface turbulence. An outline of the tests is presented in Table 5.1.

The main concern of the preliminary tests consisted of establishing the influence, if any, of the orientation of the LDV system on the measured velocities – i.e. verifying the anisotropy of the system. Therefore, two series of tests are carried out repeating the velocity measurements several times at the same fixed points, modifying only the orientation θ of the LDV probe.

In the actual tests, attention is focussed on the oscillations of the free surface and on the velocity fluctuations of the flow beneath it. In order to detect the structure of turbulence and its evolution moving away from the free surface, several velocity measurements are performed along the vertical below the water level gauge. Measurement points are closer near the surface and spread more apart as the distance from the free surface increases.

Table 5.1. Test cases

series	test	grid frequency f (Hz)	C (mm)	h (mm)	z_s (mm)	β (°) upwards	θ (°) clockwise	relative level (mm)
Preliminary tests	*test 1*	3.3	100	662	252	0	0; 90; 180; 270; 315; 225; 135; 45; 270	-50
	test 2	3.0	50	670	252	0	0; 45; 90; 135; 315	-20
		3.0	50	670	252	0	0; 45; 90; 135	-30
		3.0	50	670	252	0	0; 45; 90	-50
Actual tests	*test 3*	3.0	50	679	252	0	0	-120; .110: -100; -90; -80; -70; -60; -50; -45; -40; -35; -30; -25; -20;
	test 4	3.3	100	660	252	2.6	45	+2; +1; 0; -1; -2; -3; -4; -5; -7; -12; -15; -20; -25; -30; -40; -50; -75; -100; -125; -150
	test 5	3.3	100	660	252	2.6	45	-3; -4; -5;-6; -7; -8; -9; -10; -12; -15; -20; -25; -30; -40; -50
		3.3	100	660	252	2.6	135	-5; -10
		3.3	100	660	252	2.6	90	-10
		3.3	100	660	252	2.6	0	-10
	test 6	3.3	100	660	252	8.0	0	+2.5; +2; +1.5; +1; +0.5; 0; -1; -2; -3; -4; -5; -6; -7; -8; -9; -10; -15; -20;

6. Measurements and data analysis

Measurements of water level and local velocity are performed for all test cases.

The time series of water level are used to evaluate the statistics of the free surface oscillations. The collected velocity data are used to calculate the mean fluid velocity, the turbulent velocity fluctuations, the turbulent kinetic energy and the tangential Reynolds stresses. The results of the elaborations are reported in Appendix A.

6.1. Water level data analysis

The time series of water level are used to evaluate the statistics of the free surface fluctuations. The collected raw data are low-pass filtered to eliminate noise from the signal. The filtered time series are analysed by a zero(up)-crossing technique to evaluate the root-mean square wave height, the mean period of the fluctuations, the up- and down- midlevel amplitudes and other statistical parameters.

6.2. Velocity data analysis

The collected velocity data are used to calculate the mean fluid velocity, the turbulent velocity fluctuations, the turbulent kinetic energy and the tangential Reynolds stresses. The following paragraphs outline the analysis procedures performed on the data.

6.2.1. Transformation matrix

In order to transform the measured velocity into a velocity expressed in a fixed coordinate system, it is necessary to evaluate the transformation matrix. Let us consider the intrinsic LDV coordinate system *1-2-3* and the external coordinate system *x-y-z* and assume their relative position as shown in Figure 6.1.

The plane *1-2* is parallel to the plane of the lens of the probe and the axis *3* is the axis of the lens, passing through the measurement volume. The transformation matrix reads:

$$\begin{Bmatrix} V_1 \\ V_2 \\ V_3 \end{Bmatrix} = \begin{bmatrix} \cos\theta & \sin\theta\cos\beta & -\sin\theta\sin\beta \\ \sin\theta & -\cos\theta\cos\beta & \cos\theta\sin\beta \\ 0 & \sin\beta & \cos\beta \end{bmatrix} \begin{Bmatrix} u \\ v \\ w \end{Bmatrix} \tag{6.1}$$

and

$$\begin{Bmatrix} u \\ v \\ w \end{Bmatrix} = \begin{bmatrix} \cos\theta & \sin\theta & 0 \\ \sin\theta\cos\beta & -\cos\theta\cos\beta & \sin\beta \\ -\sin\theta\sin\beta & \cos\theta\sin\beta & \cos\beta \end{bmatrix} \begin{Bmatrix} V_1 \\ V_2 \\ V_3 \end{Bmatrix} \tag{6.2}$$

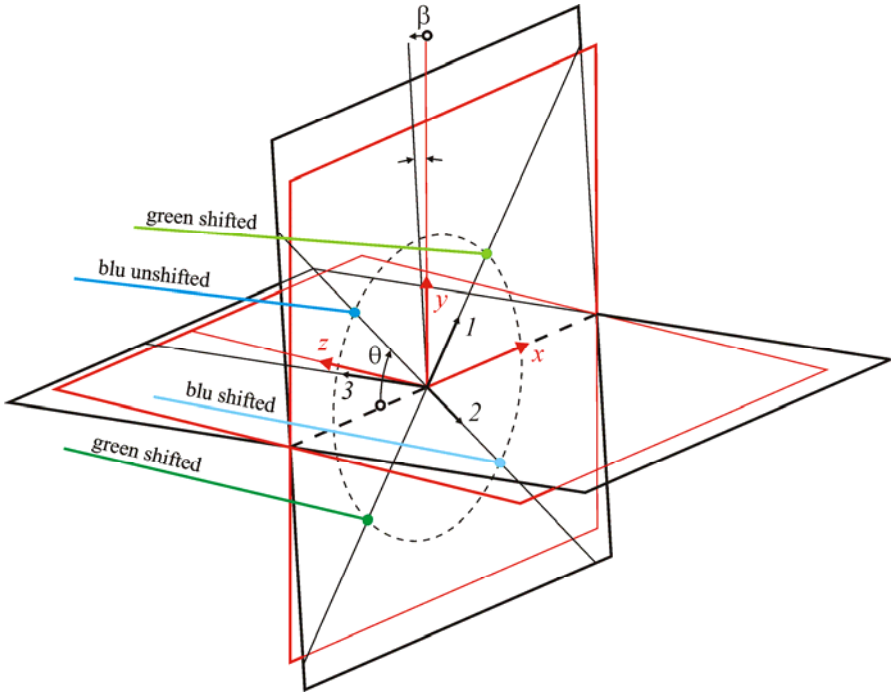

Figure 6.1. Sketch for the coordinate transformation.

If the system is a 2D measuring only V_1 and V_2, some hypothesis on the structure of the flow field are necessary for a correct transformation. If it is assumed that the motion has only components u and v, it results that V_3 is equal to $V_3 = v\sin\beta$ and, hence, the second equation in (6.2) reads:

$$v = V_1\sin\theta\cos\beta - V_2\cos\theta\cos\beta + v\sin^2\beta \rightarrow v = V_1\frac{\sin\theta}{\cos\beta} - V_2\frac{\cos\theta}{\cos\beta} \tag{6.3}$$

the two-dimensional transformation matrix becomes:

$$\begin{Bmatrix} u \\ v \end{Bmatrix} = \begin{bmatrix} \cos\theta & \sin\theta \\ \dfrac{\sin\theta}{\cos\beta} & \dfrac{\cos\theta}{\cos\beta} \end{bmatrix} \begin{Bmatrix} V_1 \\ V_2 \end{Bmatrix} \tag{6.4}$$

6.2.2. Tests on 16/04/2010

The data *run_12-run_20* refers to the same location but with different angle of laser probe. The output give several realizations of the autocorrelation $\overline{V'V'}$ (considering that the adopted LDV has two channels, each test gives the autocorrelation in two orthogonal directions, i.e. $\overline{V_1'V_1'}$ and $\overline{V_2'V_2'}$). The components of a (second-order) tensor will change under a change of coordinate system. The general rule for transforming a tensor $\mathbf{T}$ due to a change of coordinate system is $\mathbf{T}' = \mathbf{A}^T \cdot \mathbf{T} \cdot \mathbf{A}$, being A the transformation matrix between the two systems, resulting in:

$$\begin{aligned} &T_{ij}\mathbf{e}_i \otimes \mathbf{e}_j \equiv T'_{pq}\,\mathbf{e}'_p \otimes \mathbf{e}'_q = \\ &T'_{pq}\,A_{mp}\mathbf{e}_m \otimes A_{nq}\mathbf{e}_n = A_{mp}A_{nq}T'_{pq}\,\mathbf{e}_m \otimes \mathbf{e}_n \end{aligned} \tag{6.5}$$

so that:

$$T_{ij} = A_{ip}A_{jq}T'_{pq} \rightarrow T'_{ij} = A_{pi}A_{qj}T_{pq} \text{ or}$$

$$\mathbf{T} = \mathbf{A} \cdot \mathbf{T}' \cdot \mathbf{A}^T \rightarrow \mathbf{T}' = \mathbf{A}^T \cdot \mathbf{T} \cdot \mathbf{A} \tag{6.6}$$

Let us consider a coordinate system *1-2* (the LDV intrinsic system as reported in Figure 6.1) obtained by rotating a coordinate system *x-y*. The matrix of transformation is $\mathbf{A} = \begin{bmatrix} \cos\alpha & \sin\alpha \\ -\sin\alpha & \cos\alpha \end{bmatrix}$ where α is the angle between the axis *x* and the axis *1*, positive counterclockwise.

If the tensor **T** expressed in the *x-y* coordinate system is symmetric:

$$\mathbf{T}=\begin{bmatrix}\overline{u'u'} & \overline{u'v'}\\ \overline{u'v'} & \overline{v'v'}\end{bmatrix} \tag{6.7}$$

the tensor **T'** in the *1-2* coordinate system reads:

$$\begin{gathered}\mathbf{T}'=\mathbf{A}^T\cdot\mathbf{T}\cdot\mathbf{A}\rightarrow\\ \begin{bmatrix}\overline{V_1'V_1'} & \overline{V_1'V_2'}\\ \overline{V_1'V_2'} & \overline{V_2'V_2'}\end{bmatrix}=\begin{bmatrix}\cos\alpha & -\sin\alpha\\ \sin\alpha & \cos\alpha\end{bmatrix}\begin{bmatrix}\overline{u'u'} & \overline{u'v'}\\ \overline{u'v'} & \overline{v'v'}\end{bmatrix}\begin{bmatrix}\cos\alpha & \sin\alpha\\ -\sin\alpha & \cos\alpha\end{bmatrix}\rightarrow\\ \begin{cases}\overline{V_1'V_1'}=\overline{u'u'}\cos^2\alpha+\overline{v'v'}\sin^2\alpha-\overline{u'v'}\sin 2\alpha\\ \overline{V_2'V_2'}=\overline{u'u'}\sin^2\alpha+\overline{v'v'}\cos^2\alpha+\overline{u'v'}\sin 2\alpha\\ \overline{V_1'V_2'}=\frac{1}{2}\left(\overline{u'u'}-\overline{v'v'}\right)\sin 2\alpha+\overline{u'v'}\cos 2\alpha\end{cases}\end{gathered} \tag{6.8}$$

Choosing the angle $\theta=\pi/2-\alpha$ (see Figure 6.1) results:

$$\begin{cases}\overline{V_1'V_1'}=\overline{u'u'}\sin^2\theta+\overline{v'v'}\cos^2\theta-\overline{u'v'}\sin 2\theta\\ \overline{V_2'V_2'}=\overline{u'u'}\cos^2\theta+\overline{v'v'}\sin^2\theta+\overline{u'v'}\sin 2\theta\\ \overline{V_1'V_2'}=\frac{1}{2}\left(\overline{u'u'}-\overline{v'v'}\right)\sin 2\theta-\overline{u'v'}\cos 2\theta\end{cases} \tag{6.9}$$

the fitting model is: $\left(\overline{V'V'}\right)_\theta=\overline{u'u'}\sin^2\theta+\overline{v'v'}\cos^2\theta-\overline{u'v'}\sin 2\theta$.

If we have only measurements along the axis *1*, we need at least three of them at different angles $\theta_1,\theta_2,\theta_3$ to evaluate the tensor solving the following system of equations:

$$\begin{bmatrix}\sin^2\theta_1 & \cos^2\theta_1 & -\sin 2\theta_1\\ \sin^2\theta_2 & \cos^2\theta_2 & -\sin 2\theta_2\\ \sin^2\theta_3 & \cos^2\theta_3 & -\sin 2\theta_3\end{bmatrix}\begin{Bmatrix}\overline{u'u'}\\ \overline{v'v'}\\ \overline{u'v'}\end{Bmatrix}=\begin{Bmatrix}\left(\overline{V_1'V_1'}\right)_1\\ \left(\overline{V_1'V_1'}\right)_2\\ \left(\overline{V_1'V_1'}\right)_3\end{Bmatrix} \tag{6.10}$$

With more than three measurements we can evaluate the best fitting tensor. If we have also measurements of the cross-correlation $\overline{V_1'V_2'}$, we can include new equations and best fit the tensor involved in the general following system of equations:

$$\begin{bmatrix} \sin^2\theta_1 & \cos^2\theta_1 & -\sin 2\theta_1 \\ \vdots & \vdots & \vdots \\ \sin^2\theta_N & \cos^2\theta_N & -\sin 2\theta_N \\ \frac{1}{2}\sin 2\theta_{N+1} & -\frac{1}{2}\sin 2\theta_{N+1} & -\cos 2\theta_{N+1} \\ \vdots & \vdots & \vdots \\ \frac{1}{2}\sin 2\theta_{N+K} & -\frac{1}{2}\sin 2\theta_{N+K} & -\cos 2\theta_{N+K} \end{bmatrix} \begin{Bmatrix} \overline{u'u'} \\ \overline{v'v'} \\ \overline{u'v'} \end{Bmatrix} = \begin{Bmatrix} \left(\overline{V_1'V_1'}\right)_1 \\ \vdots \\ \left(\overline{V_1'V_1'}\right)_N \\ \left(\overline{V_1'V_2'}\right)_1 \\ \vdots \\ \left(\overline{V_1'V_2'}\right)_K \end{Bmatrix} \tag{6.11}$$

On using the output results from *run_12* to *run_20* in coincidence mode, the result of the best fitting is:

$$\begin{aligned} \overline{u'u'} &= 3.72\cdot 10^{-3}\ \mathrm{m^2/s^2} \\ \overline{v'v'} &= 3.00\cdot 10^{-3}\ \mathrm{m^2/s^2} \\ \overline{u'v'} &= -3.48\cdot 10^{-4}\ \mathrm{m^2/s^2} \end{aligned} \tag{6.12}$$

The best fitting curve and the raw data are reported in Figure 6.2.

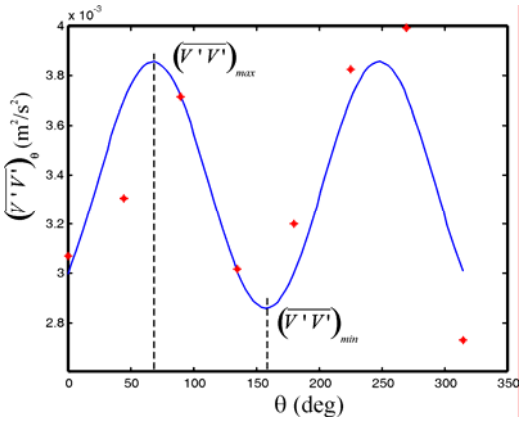

Figure 6.2. Best fitting curve and measured data

The maximum and minimum values of the autocorrelation are computed as

$$\overline{V'V'} = \frac{\overline{u'u'} + \overline{v'v'}}{2} \pm \sqrt{\left(\frac{\overline{u'u'} - \overline{v'v'}}{2} \right)^2 + \overline{u'v'}^2} \tag{6.13}$$

and the axis angle of their occurrence is

$$\alpha = \frac{1}{2} \tan^{-1} \left(\frac{2\overline{u'v'}}{\overline{u'u'} - \overline{v'v'}} \right) \tag{6.14}$$

and its orthogonal. The computed values are

$$\begin{aligned} \left(\overline{V'V'} \right)_{max} &= 3.86 \cdot 10^{-3} \ \mathrm{m^2/s^2} \\ \left(\overline{V'V'} \right)_{min} &= 2.86 \cdot 10^{-3} \ \mathrm{m^2/s^2} \end{aligned} \tag{6.15}$$

and $\alpha \simeq -22^\circ \rightarrow \theta \simeq 68^\circ ; 158^\circ$.

Turbulence structure, as expressed from this tensor, is far from isotropic; whereas it should be almost isotropic.

A further analysis has been carried out assuming that the mean velocity is not constant but slowly varying. The fluctuating component is defined as $V' = V(t) - \overline{V}(t)$ where $\overline{V}(t)$ is computed as the moving average of the instantaneous velocity. As a first attempt, the window of time average is assumed equal to 1 s. In Figure 6.3 the instantaneous and the moving average velocities (1 s average) are shown.

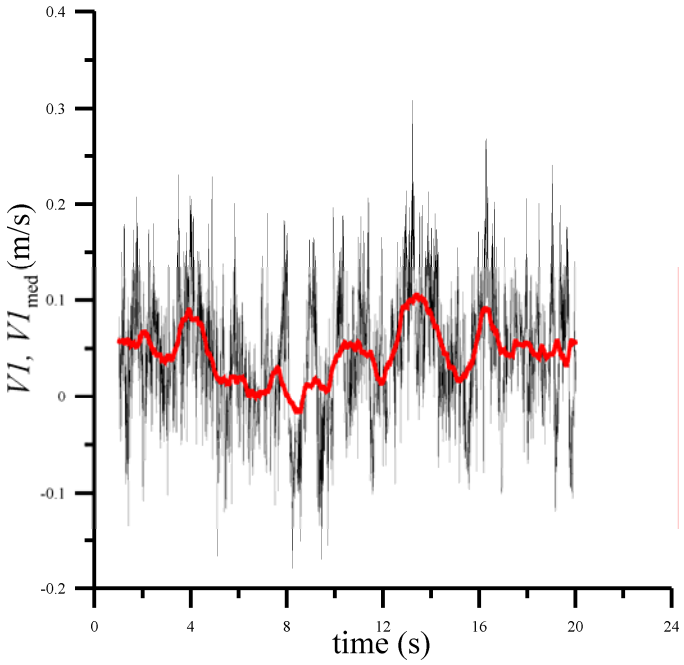

Figure 6.3. Instantaneous velocity and low pass filtered (moving average) velocity for channel 1, run_12.

The mean velocity is clearly time varying, with period of a few seconds. On using this different evaluation of turbulence, the following data are computed:

$$\begin{aligned}\overline{u'u'} &= 2.53\cdot10^{-3}\ \mathrm{m^2/s^2}\\ \overline{v'v'} &= 2.56\cdot10^{-3}\ \mathrm{m^2/s^2}\\ \overline{u'v'} &= -4.2\cdot10^{-5}\ \mathrm{m^2/s^2}\end{aligned} \qquad (6.16)$$

hence

$$\begin{aligned}\left(\overline{V'V'}\right)_{max} &= 2.59\cdot10^{-3}\ \mathrm{m^2/s^2}\\ \left(\overline{V'V'}\right)_{min} &= 2.50\cdot10^{-3}\ \mathrm{m^2/s^2}\end{aligned} \qquad (6.17)$$

and finally $\alpha \simeq -34^\circ \rightarrow \theta \simeq 56^\circ;146^\circ$

The stress tensor is almost diagonal, with a negligible non diagonal contribution, and almost isotropic. The trace of the tensor, proportional to the Turbulent Kinetic

Energy, is smaller, as expected due to the elimination of the long period (longer than 1 s) contribution.

In order to have a criterion for choosing the proper time interval for averaging t_{ave}, the analysis has been extended to different values of t_{ave}. The results are reported in Table 6.1 in terms of the Reynolds stresses and of the parameters STD and R^2.

STD is a measure of anisotropy (equal to zero for perfect isotropy) and it is defined as

$$STD = \frac{1}{\left(\overline{V'V'}\right)_{ave}} \sqrt{\left[\left(\overline{V'V'}\right)_{max} - \left(\overline{V'V'}\right)_{ave}\right]^2 + \left[\left(\overline{V'V'}\right)_{min} - \left(\overline{V'V'}\right)_{ave}\right]^2} \qquad (6.18)$$

while R^2 is the coefficient of determination of the best fitting. Note that STD has a minimum almost coincident with the maximum R^2. The optimal size of the window of time average is say 1.5 s.

Table 6.1. Results of the best fitting model for different values of t_{ave}

t_{ave}	$\overline{u'u'}$	$\overline{v'v'}$	$\overline{u'v'}$	α	$\left(\overline{V'V'}\right)_{max}$	$\left(\overline{V'V'}\right)_{min}$	$\left(\overline{V'V'}\right)_{ave}$	STD	R^2
(s)	(m^2/s^2)	(m^2/s^2)	(m^2/s^2)	(°)	(m^2/s^2)	(m^2/s^2)	(m^2/s^2)	(.)	(.)
0.33	0.00184	0.00196	4.94E-05	-20	0.00197	0.00182	0.00189	5.51%	0.27
0.5	0.00209	0.00219	4.91E-05	-23	0.00221	0.00207	0.00214	4.59%	0.17
1.0	0.00253	0.00256	-4.29 E-05	35	0.00259	0.00250	0.00255	2.50%	0.23
1.25	0.00268	0.00267	1.57E-05	36	0.00269	0.00266	0.00267	0.88%	0.55
1.5	0.00280	0.00277	6.88E-06	16	0.00280	0.00277	0.00278	0.65%	0.77
1.75	0.00290	0.00286	-1.79E-07	0	0.00290	0.00286	0.00288	0.78%	0.98
2.0	0.00298	0.00291	-2.12E-05	-15	0.00298	0.00290	0.00294	1.99%	0.86
2.5	0.00310	0.00299	-4.49E-05	-20	0.00312	0.00298	0.00305	3.25%	0.18
3.0	0.00320	0.00306	-6.14E-05	-20	0.00323	0.00304	0.00313	4.30%	0.62

Essentially this is a new technique for turbulence detection in a wide class of turbulent flows, and is much more physically based than a simple filtering of the data.

Conclusions

Some tests on grid turbulence as interacting with free surface have been carried out. Presently only the test case has been analysed in detail, and a novel technique for turbulence separation from potential flow contribution has been detected. It is based on the structure of the Reynolds tensor, which has to respect the transformation rules if the coordinate system is changed. The technique has been applied assuming isotropicity in the stress tensor, but this last condition can be relaxed making it viable for several different flow fields.

Acknowledgements

The tests were carried out in CEAMA, in Granada. The experimental activity was carried out by Mara Tonelli during her visit at CEAMA from end March to end April 2010, and by Sandro Longo during his sabbatical leave from 1st March to 30th July. The grid and part of the instrumentation was prepared and tested in situ by Luca Chiapponi, during his numerous visits in Granada. Many thanks to all the staff from CEAMA for their availability to host the activity and the permanence of the mentioned authors. Special thanks to Maria Clavero, responsible of the flume in the lab, and to Antonio Monino for his numerous advices and suggestions.

7. References

Adrian, R.J., Yao, C.S. (1987). Power spectra of fluid velocities measured by laser Doppler velocimetry Exp. Fluids, 5, pp.17.

Battjes J.A., Sakai T. (1981). Velocity field in a steady breaker. J Fluid Mech 111: 421-437

Benedict, L.H., Nobach, H., Tropea, C. (2000). Estimation of turbulent velocity spectra from laser Doppler data. Meas. Sci. Technol., 11, 1089-1104

Brocchini M, Peregrine D.H. (2001a). The dynamics of strong turbulence at free surfaces. Part 1. Description. J Fluid Mech 449: 225-254

Brocchini M., Peregrine D.H. (2001b). The dynamics of strong turbulence at free surfaces. Part 2. Free-surface boundary conditions. J Fluid Mech 449: 255-290

Brumley B.H., Jirka G.H. (1983). Near-surface turbulence in a grid-stirred tank. J Fluid Mech 183: 235-263

Dabiri D., Gharib M. (2001). Simultaneous free-surface deformation and near-surface velocity measurements. Exp Fluids 30: 381-390

Dankwerts, P.V. (1951). Significance of Liquid-Film Coefficients in Gas Absorption. Ind Eng Chem, 43, 1460, 1951

Driver, D.M., Seegmiller, H.L. (1985). Features of a reattaching turbulent shear layer in divergent channel flow. AIAA Journal, 23(2), 163-171

Durão, D.F.G., Laker, J., Whitelaw, J.H. (1980). Bias effects in laser Doppler anemometry. J. Phys. E: Sci. Instrum., 13, 442-445

Edwards, R.V. (1987). Report of the special panel on statistical particle bias problems in laser anemometry. Trans. of the ASME, J. of Fluids Eng., 109, 89-93

George, W.K., Lumley, J.L. (1973). The laser Doppler velocimeter and its application to the measurement of turbulence. J. Fluid Mech., 60, 321-362

Higbie, R. (1935). The Rate of Absorption of a Pure Gas into a Still Liquid During Short Periods of Exposure. AIChE Trans, 31, 365, 1935

Hoesel, W., Rodi, W. (1977). New biasing elimination method for laser-Doppler-velocimeter counter processing. Rev. Sci. Instrum., 910-919

Hong W-L., Walker D.T. (2000). Reynolds-averaged equations for free-surface flows with application to high-Froude number jet spreading. J Fluid Mech 417: 183-209

Komori S., Murakami Y., Ueda H. (1989). The relationship between surface-renewal and bursting motions in an open-channel flow. J Fluid Mech 203: 102-123

Komori, S., Murakami, Y., Ueda, H. (1989). The relationship between surface-renewal and bursting motions in an open-channel flow. J. Fluid Mech., 203, 102-123

Longo, S., (2010). Experiments on turbulence beneath a free surface in a stationary field generated by a Crump weir: free surface characteristics and the relevant scales. Experiments in Fluids, Springer, DOI: 10.1007/s00348-010-0881-5

Longo, S., (2010). Experiments on turbulence beneath a free surface in a stationary field generated by a Crump weir: turbulence structure and correlation with the free surface. Experiments in Fluids, Springer, DOI: 10.1007/s00348-010-0921-1

McCready M.A., Vassiliadou E., Hanratty T.J. (1986). Computer Simulation of Turbulent Mass Transfer at a Mobile Interface. AIChE J, 32, 1108, 1986

McLaughlin, D.K., Tiederman, W.G. (1973). Biasing correction for individual realization of laser anemometer measurements in turbulent flows. Phys. of Fluids, 16(12), 2082-2088

Nakagawa H.I., Nezu I. (1977). Predictions of the contributions to the Reynolds stress from the bursting events in open channel flows. J Fluid Mech 80: 99-128

Nezu, I., Rodi, W. (1986). Open channel flow measurement with LDA. J. Hydr. Eng., 112(5), 335-355

Nobach, H. (1999). Processing of stochastic sampled data in laser Doppler anemometry. Proc. of the 3rd Int. Workshop on Sampling theory and applications, Trondheim, 149-154.

Orlins, J.J., Gulliver, J.S. (2003). Turbulence quantification and sediment resuspension in an oscillating grid chamber. Exp. Fluids, 34, 662-677

Phillips O.M. (1957). On the generation of waves by turbulent wind. J Fluid Mech 2: 417-445

Quiao H.B., Duncan J.H. (2001). Gentle spilling breakers: crest flow-field evolution. J Fluid Mech 439: 57-85

Ramond, A., Millan, P. (2000). Measurement and treatment of LDA signals, comparison with hot-wire signals. Exp. Fluids, 28, 58-63

Savelsberg R., Holten A., van de Water W. (2006). Measurement of the gradient field of a turbulent free surface. Exp Fluids 41 (4): 629-640

Settles G. (2001). Schlieren and Shadowgraph techniques, visualizing phenomena in transparent media. Springer, Berlin Heidelberg New York

Shen L., Yue D.K.P. (2001). Large-eddy simulation of free-surface turbulence. J Fluid Mech 440: 75-116

Shen L., Zhang X., Yue D.K.P., Triantafyllou G.S. (1999). The surface layer for free-surface turbulent flows. J Fluid Mech 386: 167-212

Sirkar K.K., Hanratty T.J. (1970). Turbulent Mass Transfer Rates to a Wall for Large Schmidt Numbers to the Velocity Field. J Fluid Mech, 44, 598, 1970

Tamburrino A., Gulliver J.S. (1999). Large flow structures in a turbulent open-channel flow, J. Hydraul. Res., 37(3), 363- 380

Tamburrino A., Gulliver J.S. (2002). Free-surface turbulence and mass transfer in a channel flow, AIChE J., 48(12), 2732- 2743

Teixeira M.A.C., Belcher S.E. (2006). The initial generation of surface waves by turbulent shear flow, Dynamics of Atmosphere and Oceans, 41, 1-27

Walker, D.T., Chen, C.-Y., Willmarth, W.W. (1995). Turbulent structure in free-surface jet flows. J. Fluid. Mech., 291, 223-261

Weingand A. (1996). Simultaneous mapping of the velocity and deformation field at a free surface. Exp Fluids 20: 358-364

Yeh, Y., Cummins, H.Z. (1964). Localized fluid flow measurements with an He-Ne Laser Spectrometer. Appl. Phys. Lett., 4, 176-178

Appendix A

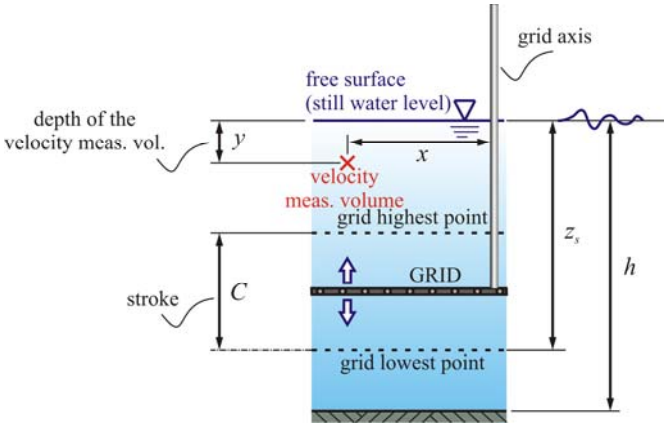

Figure A.1. Reference system for LDV 2D measurements

LEGENDA of the files

<filename>.set	→	LDV file containing the set-up of Flowsizer™
<filename>.dat	→	LDV file containing the rough data from FSA3500
<filename>	→	file ASCII containing the LDV data for the NON coincidence mode
<filename>_bis	→	file ASCII containing the LDV data for the coincidence mode
<filename>_elab.mat	→	file matlab containing the LDV data as exported in the ASCII file corrected for time trigger
<filename>.daq	→	file containing the raw data from Matlab as acquired on using NIDAQ (US level and grid position, in Volt); can be downloaded in Matlab with the command daqread(<nomefile>)
<filename>.log	→	file containing several information on NIDAQ acquisition and on the structure of the output files
<filename>lev_elab.mat	→	file matlab containing the NIDAQ data (time, grid position in Volt and water level distance from the US sensor in mm) corrected for time trigger

Table A.1. Water velocity measurements. Stroke ±50 mm

file name (non coinc. mode)	data rate Ch 1 (non coinc. mode) (Hz)	data rate Ch 2 (non coinc. mode) (Hz)	file name (coinc. mode)	data rate (coinc. mode) (Hz)	date (gg/mm/aaaa)	C (mm)	h (mm)	z_s (mm)	grid frequency f (Hz)	relative level (mm)	duration (s)	comments
run_0	NA	NA	NA	NA	NA	NA	NA	NA	NA	NA	NA	only NIDAQ file for still water level
run_12	530	196	run_12_bis	35	16/04/2010	100	662	252	3.3	-50	137	probe angle θ = 0°
run_13	704	300	run_13_bis	41	16/04/2010	100	662	252	3.3	-50	99	probe angle 90° (clockwise)
run_14	762	324	run_14_bis	54	16/04/2010	100	662	252	3.3	-50	92	probe angle 180° (clockwise)
run_15	865	319	run_15_bis	54	16/04/2010	100	662	252	3.3	-50	84	probe angle 270° (clockwise) – N.B. water level and grid position file not available
run_16	837	306	run_16_bis	51	16/04/2010	100	662	252	3.3	-50	87	probe angle 315° (clockwise)

run_17	815	319	run_17_bis	54	16/04/2010	100	662	252	3.3	-50	88	probe angle 225° (clockwise)
run_18	814	313	run_18_bis	53	16/04/2010	100	662	252	3.3	-50	88	probe angle 135° (clockwise)
run_19	857	317	run_19_bis	57	16/04/2010	100	662	252	3.3	-50	85	probe angle 45° (clockwise)
run_20	897	299	run_20_bis	53	16/04/2010	100	662	252	3.3	-50	82	probe angle 270° (clockwise)

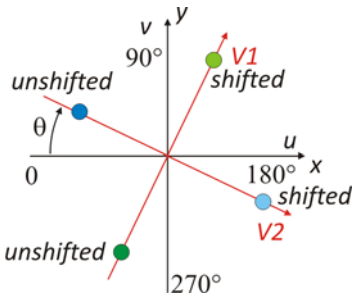

Figure A.2. Reference system for the laser and external (*x*-*y*). θ is the probe angle, *V1* and *V2* are the LDV velocity output for channel 1 (green) and channel 2 (blue). *u* and *v* are velocity in the external reference system

$$\begin{Bmatrix} V1 \\ V2 \end{Bmatrix} = \begin{bmatrix} \sin\theta & \cos\theta \\ \cos\theta & -\sin\theta \end{bmatrix} \begin{Bmatrix} u \\ v \end{Bmatrix}$$

Figure A.3. Transformation matrix for β = 0°

Table A.2. Output for water velocity measurements, coincidence mode. Volume of measurements at -50 mm (respect to the still water level) and 50 mm off respect to the grid axis

file name	*V1* (m/s)	*V2* (m/s)	$V1_{rms}$ (m/s)	$V2_{rms}$ (m/s)	*u* (m/s)	*v* (m/s)	u_{rms} (m/s)	v_{rms} (m/s)	$(u'v')_{rms}$ (m^2/s^2)	*k* (m^2/s^2)	ø (°)
run_12_bis	0.033315	0.053001	0.052835	0.064308	0.058437	0.037508	0.070528	0.058147	0.000996	0.004178	-16.0
run_13_bis	0.056388	-0.03191	0.059602	0.055736	0.064808	0.036829	0.063323	0.063224	0.000692	0.004004	-44.5
run_14_bis	-0.03054	-0.04997	0.056887	0.06928	0.049971	0.030543	0.06928	0.056887	0.000783	0.004018	-13.3

run_15_bis	-0.04191	0.030129	0.064756	0.062063	0.041905	0.030129	0.064756	0.062063	0.000637	0.004023	-30.9
run_16_bis	0.004763	0.032054	0.048115	0.056386	0.02591	0.029827	0.062906	0.055963	0.00059	0.003545	-17.8
run_17_bis	-0.04641	-0.00526	0.060342	0.061064	0.03654	0.029099	0.063256	0.058059	-4.4E-05	0.003686	2.0
run_18_bis	0.013471	-0.05956	0.056449	0.064699	0.051652	0.032598	0.062785	0.058589	0.0005	0.003687	-22.2
run_19_bis	0.045086	-0.00026	0.057515	0.049215	0.040775	0.037038	0.065533	0.056562	0.000297	0.003747	-7.6
run_20_bis	-0.06464	0.03454	0.056614	0.055036	0.071434	0.037766	0.062212	0.063568	0.000702	0.003956	38.2

Data acquisition from NIDAQ (US level and grid position) send a trigger signal to the FSA3500 which restart the time stamp from zero. On using the software elaborazione_laser.m the data from LDV were conditioned eliminating the interval time before triggering signal and were saved in .mat files.

Table A.3. Water velocity measurements. x = -50 mm, probe angle θ = 0°, Stroke ±25 mm

file name (non coinc. mode)	data rate Ch 1 (non coinc. mode) (Hz)	data rate Ch 2 (non coinc. mode) (Hz)	file name (coinc. mode)	data rate (coinc. mode) (Hz)	date (gg/mm/aaaa)	C (mm)	h (mm)	z_s (mm)	grid frequency f (Hz)	relative level (mm)	duration (s)	comments
run_21	589	137	run_21_bis	26	19/04/2010	50	679	252	3.0	-50	413	anomalous setup
run_22	541	130	run_22_bis	26	19/04/2010	50	679	252	3.0	-45	210	anomalous setup
run_23	524	135	run_23_bis	26	19/04/2010	50	679	252	3.0	-40	221	anomalous setup
run_24	638	188	run_24_bis	24	19/04/2010	50	679	252	3.0	-35	244	
run_25	567	183	run_25_bis	21	19/04/2010	50	679	252	3.0	-30	257	
run_26	550	176	run_26_bis	13	19/04/2010	50	679	252	3.0	-25	258	
run_27	569	175	run_27_bis	12	19/04/2010	50	679	252	3.0	-20	301	
run_28	647	184	run_28_bis	28	19/04/2010	50	679	252	3.0	-40	252	
run_29	661	181	run_29_bis	28	19/04/2010	50	679	252	3.0	-45	249	
run_30	619	168	run_30_bis	17	19/04/2010	50	679	252	3.0	-120	272	
run_31	624	154	run_31_bis	17	19/04/2010	50	679	252	3.0	-120	249	
run_32	585	118	run_32_bis	14	19/04/2010	50	679	252	3.0	-110	250	
run_33	609	132	run_33_bis	14	19/04/2010	50	679	252	3.0	-100	253	
run_34	616	137	run_34_bis	15	19/04/2010	50	679	252	3.0	-90	299	
run_35	557	155	run_35_bis	18	19/04/2010	50	679	252	3.0	-80	250	
run_36	683	151	run_36_bis	22	19/04/2010	50	679	252	3.0	-60	253	
run_37	632	164	run_37_bis	19	19/04/2010	50	679	252	3.0	-70	250	
run_38	NA	NA	run_38_bis	NA	19/04/2010	50	679	252	3.0	NA	NA	grid stopped – file LDV non existent

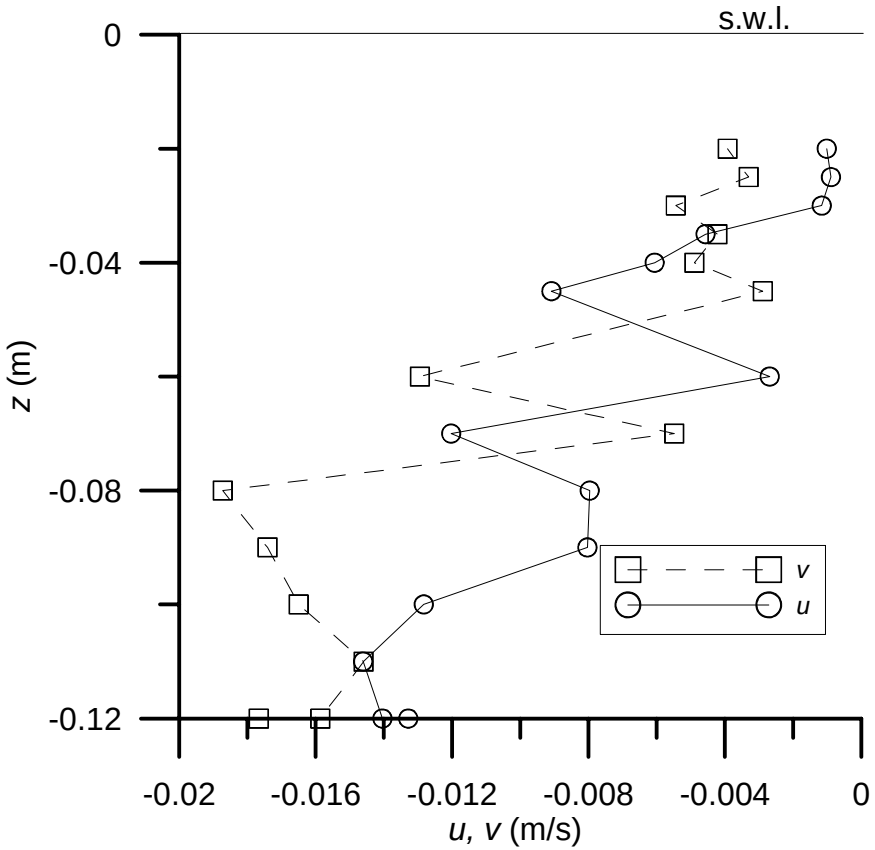

Figure A.4. Mean horizontal (*u*) and vertical (*v*) velocity profile

Table A.4. Water velocity measurements. x = -100 mm. Stroke ±25 mm

file name (non coinc. mode)	data rate Ch 1 (non coinc. mode) (Hz)	data rate Ch 2 (non coinc. mode) (Hz)	file name (coinc. mode)	data rate (coinc. mode) (Hz)	date (gg/mm/aaaa)	C (mm)	h (mm)	z_s (mm)	grid frequency f (Hz)	relative level (mm)	duration (s)	comments
run_39	NA	NA	run_39_bis	NA	20/04/2010	100	670	252	3.0	-20	NA	probe angle θ = 0° DAT file not available for new elaboration
run_40	651	257	run_40_bis	39	20/04/2010	100	670	252	3.0	-20	255	probe angle 90° (clockwise)
run_41	644	216	run_41_bis	27	20/04/2010	100	670	252	3.0	-20	263	probe angle 135° (clockwise)
run_42	445	120	run_42_bis	14	20/04/2010	100	670	252	3.0	-20	250	probe angle 135° (clockwise)
run_43	441	123	run_43_bis	16	20/04/2010	100	670	252	3.0	-20	256	probe angle 315° (clockwise)
run_44	399	118	run_44_bis	14	20/04/2010	100	670	252	3.0	-20	249	probe angle 315° (clockwise)
run_45	424	152	run_45_bis	10	20/04/2010	100	670	252	3.0	-20	270	probe angle 0° (clockwise)
run_46	494	149	run_46_bis	22	20/04/2010	100	670	252	3.0	-20	252	probe angle 90° (clockwise)
run_47	498	144	run_47_bis	18	20/04/2010	100	670	252	3.0	-30	251	probe angle 90° (clockwise)
run_48	474	149	run_48_bis	15	20/04/2010	100	670	252	3.0	-30	251	probe angle 0° (clockwise)
run_49	512	144	run_49_bis	18	20/04/2010	100	670	252	3.0	-30	253	probe angle 45° (clockwise)
run_50	437	119	run_50_bis	13	20/04/2010	100	670	252	3.0	-20	250	probe angle 45° (clockwise)
run_51	423	112	run_51_bis	14	20/04/2010	100	670	252	3.0	-20	254	probe angle 45° (clockwise)
run_52	476	140	run_52_bis	18	20/04/2010	100	670	252	3.0	-30	250	probe angle 135° (clockwise)
run_53	428	138	run_53_bis	16	20/04/2010	100	670	252	3.0	-50	252	probe angle 135° (clockwise)
run_54	509	122	run_54_bis	17	20/04/2010	100	670	252	3.0	-50	253	probe angle 0° (clockwise)
run_55	378	96	run_55_bis	10	20/04/2010	100	670	252	3.0	-50	356	probe angle 90° (clockwise) Long no-burst interval after 250 s

run_56	NA	NA	run_56_bis	NA	20/04/2010	100	670	252	3.0	-50	NA	probe angle 45° (clockwise) Data file corrupted

Table A.5. Water velocity measurements. x = -50 mm. Stroke ±50 mm

file name (non coinc. mode)	data rate Ch 1 (non coinc. mode) (Hz)	data rate Ch 2 (non coinc. mode) (Hz)	file name (coinc. mode)	data rate (coinc. mode) (Hz)	date (gg/mm/aaaa)	C (mm)	h (mm)	z_s (mm)	grid frequency f (Hz)	relative level (mm)	duration (s)	comments
run_57	NA	NA	run_57_bis	NA	22/04/2010	100	660	252	3.3	0	NA	probe angle θ = 45° DAT file not available for new elaboration
run_58	NA	NA	run_58_bis	NA	22/04/2010	100	660	252	3.3	0	NA	probe angle θ = 45° DAT file not available for new elaboration
run_59	232	86	run_59_bis	15	22/04/2010	100	660	252	3.3	0	271	probe angle θ = 45°, β = 2.6° (upward)
run_60	234	91	run_60_bis	16	22/04/2010	100	660	252	3.3	-1	250	probe angle θ = 45°, β = 2.6° (upward)
run_61	237	85	run_61_bis	16	22/04/2010	100	660	252	3.3	1	253	probe angle θ = 45°, β = 2.6° (upward)
run_62	220	74	run_62_bis	14	22/04/2010	100	660	252	3.3	2	251	probe angle θ = 45°, β = 2.6° (upward)
run_63	251	87	run_63_bis	16	22/04/2010	100	660	252	3.3	-2	251	probe angle θ = 45°, β = 2.6° (upward)
run_64	252	87	run_64_bis	16	22/04/2010	100	660	252	3.3	-3	249	probe angle θ = 45°, β = 2.6° (upward)
run_65	267	85	run_65_bis	16	22/04/2010	100	660	252	3.3	-4	252	probe angle θ = 45°, β = 2.6° (upward)
run_66	253	89	run_66_bis	16	22/04/2010	100	660	252	3.3	-5	250	probe angle θ = 45°, β = 2.6° (upward)
run_67	254	86	run_67_bis	16	22/04/2010	100	660	252	3.3	-7	249	probe angle θ = 45°, β = 2.6° (upward)
run_68	228	90	run_68_bis	15	22/04/2010	100	660	252	3.3	-9	249	probe angle θ = 45°, β = 2.6° (upward)
run_69	199	87	run_69_bis	14	22/04/2010	100	660	252	3.3	-12	247	probe angle θ = 45°, β = 2.6° (upward)
run_70	175	86	run_70_bis	13	22/04/2010	100	660	252	3.3	-15	258	probe angle θ = 45°, β = 2.6° (upward)
run_71	172	86	run_71_bis	13	22/04/2010	100	660	252	3.3	-20	262	probe angle θ = 45°, β = 2.6° (upward)
run_72	168	82	run_72_bis	13	22/04/2010	100	660	252	3.3	-25	256	probe angle θ = 45°, β = 2.6° (upward)
run_73	160	90	run_73_bis	13	22/04/2010	100	660	252	3.3	-30	248	probe angle θ = 45°, β = 2.6° (upward)
run_74	181	99	run_74_bis	15	22/04/2010	100	660	252	3.3	-40	251	probe angle θ = 45°, β = 2.6° (upward)

run_75	182	97	run_75_bis	14	22/04/2010	100	660	252	3.3	-50	247	probe angle θ = 45°, β = 2.6° (upward)
run_76	188	106	run_76_bis	16	22/04/2010	100	660	252	3.3	-75	251	probe angle θ = 45°, β = 2.6° (upward)
run_77	190	103	run_77_bis	17	22/04/2010	100	660	252	3.3	-100	256	probe angle θ = 45°, β = 2.6° (upward)
run_78	195	103	run_78_bis	19	22/04/2010	100	660	252	3.3	-125	260	probe angle θ = 45°, β = 2.6° (upward)
run_79	154	79	run_79_bis		22/04/2010	100	660	252	3.3	-150	260	probe angle θ = 45°, β = 2.6° (upward)

Table A.6. Output for water velocity measurements. x = -50 mm. Stroke ±50 mm

	z (m)	$V1$ (m/s)	$V2$ (m/s)	$V1_{rms}$ (m/s)	$V2_{rms}$ (m/s)	u (m/s)	v (m/s)	u_{rms} (m/s)	v_{rms} (m/s)	$(u'v')_{rms}$ (m^2/s^2)	k (m^2/s^2)	ø (°)
run_79	-0.15	0.061443	-0.04716	0.107984	0.152964	0.013315	0.072693	0.160976	0.177617	-0.00871	0.028731	-28.5
run_78	-0.125	0.108872	-0.08692	0.057515	0.064283	0.020514	0.140143	0.066991	0.065627	-0.00048	0.004397	34.7
run_77	-0.1	0.106912	-0.0782	0.045096	0.047607	0.022474	0.133519	0.054709	0.053122	-0.00046	0.002908	34.7
run_76	-0.075	0.075852	-0.05427	0.051118	0.049812	0.017454	0.098153	0.053038	0.059669	-0.00017	0.003187	-6.5
run_75	-0.05	0.039328	-0.03831	0.063107	0.052468	0.004163	0.062056	0.062417	0.069101	0.000224	0.004335	7.1
run_74	-0.04	0.018536	-0.03425	0.063209	0.055642	-0.01018	0.040594	0.063844	0.070322	0.000379	0.004511	11.8
run_73	-0.03	0.017276	-0.02893	0.062379	0.054617	-0.0079	0.031819	0.063477	0.06958	0.000252	0.004435	8.6
run_72	-0.025	0.0047	-0.0169	0.066148	0.066091	-0.00756	0.017954	0.067511	0.077153	0.000116	0.005255	2.4
run_71	-0.02	0.018914	-0.0051	0.063226	0.056172	0.009582	0.020927	0.065237	0.070826	0.000121	0.004636	4.5
run_70	-0.015	0.029135	0.003939	0.057114	0.059591	0.024561	0.016877	0.063789	0.06745	-0.00031	0.004309	-16.2
run_69	-0.012	0.022313	0.012129	0.060472	0.0637	0.030027	0.005646	0.069178	0.07159	-0.00063	0.004955	-30.9
run_68	-0.009	0.037724	0.023201	0.058746	0.059559	0.048108	0.011774	0.069856	0.067243	-0.0007	0.004701	31.4
run_67	-0.007	0.039353	0.018064	0.055379	0.061769	0.048367	0.011725	0.072674	0.061853	-0.00091	0.004554	15.9
run_66	-0.005	0.033456	0.022101	0.057079	0.062308	0.046836	0.009074	0.074008	0.059424	-0.00062	0.004504	8.9
run_65	-0.004	0.044971	0.036447	0.0537	0.058714	0.063785	0.00281	0.068186	0.058816	-0.00059	0.004054	13.2
run_64	-0.003	0.032557	0.026662	0.057671	0.063508	0.05237	0.002746	0.078871	0.05634	-0.00064	0.004697	6.0
run_63	-0.002	0.043204	0.033481	0.059763	0.06194	0.060762	0.0035	0.082049	0.055588	-0.00062	0.004911	4.8
run_60	-0.001	0.042207	0.031921	0.057917	0.067238	0.063981	0.003555	0.081038	0.054437	-0.00072	0.004765	5.6
run_59	0	0.037816	0.024876	0.059415	0.063941	0.054197	0.00582	0.08602	0.0503	-0.00056	0.004965	3.3
run_61	0.001	0.045989	0.040633	0.056423	0.062707	0.072989	0.00249	0.07955	0.049408	-0.0007	0.004385	5.1
run_62	0.002	0.038884	0.042315	0.056998	0.062334	0.062844	0.003395	0.08937	0.062002	-0.00221	0.005916	14.0

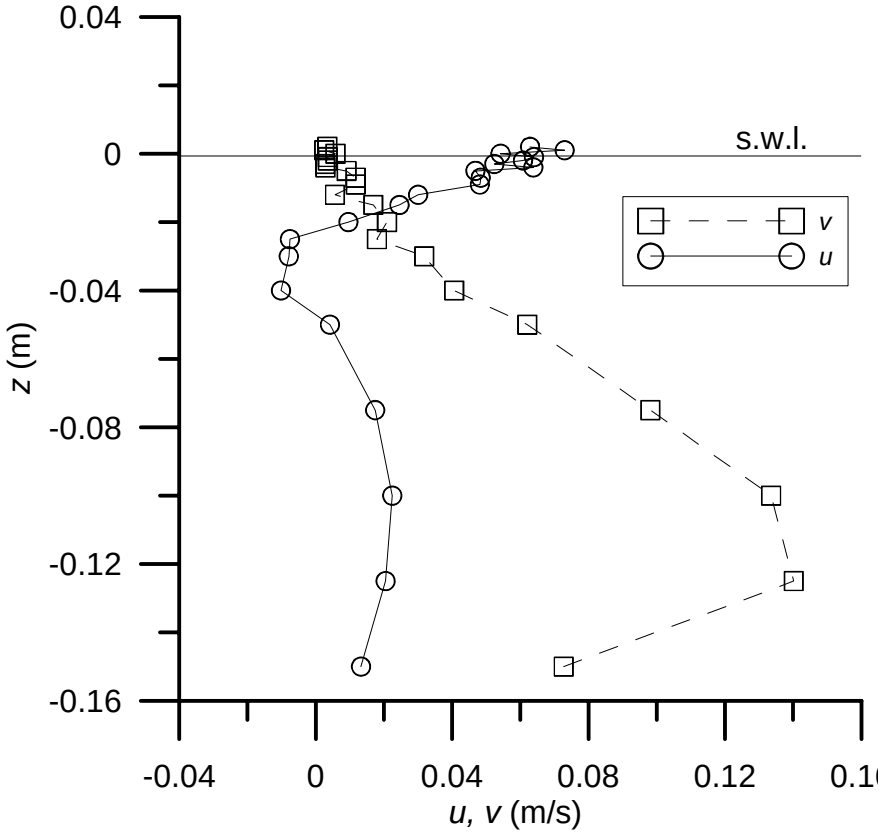

Figure A.5. Mean horizontal (*u*) and vertical (*v*) velocity profile

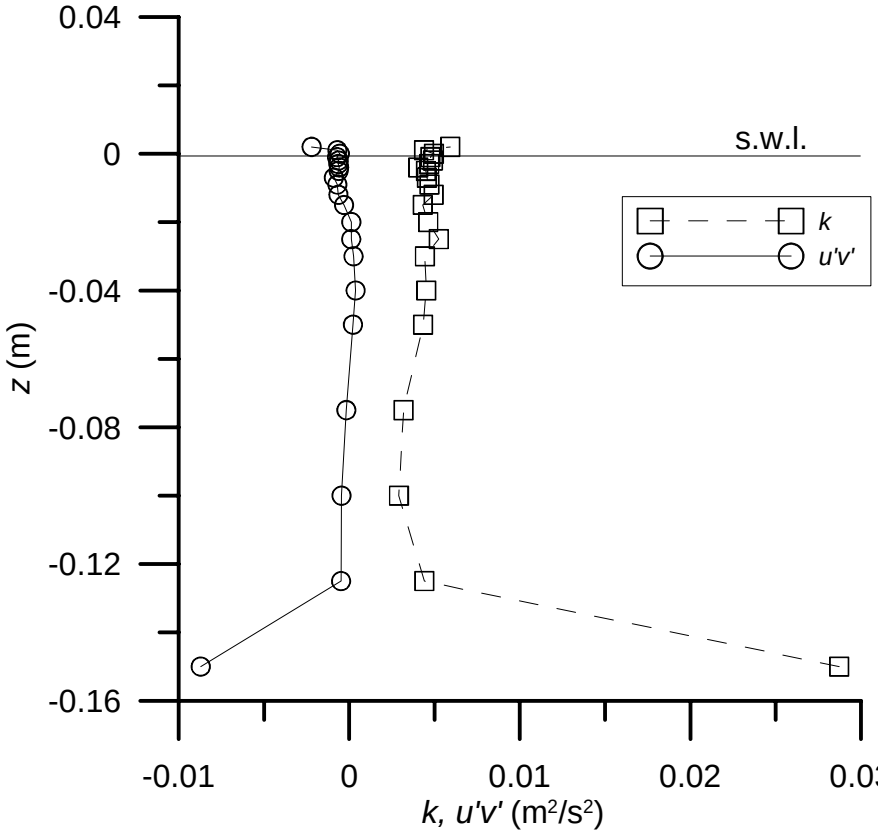

Figure A.6. Turbulent kinetic energy (*k*) and Reynolds tangential stress (*u'v'*) profile.

Table A.7. Water velocity measurements. x = -50 mm. Stroke ±50 mm

file name (non coinc. mode)	data rate Ch 1 (non coinc. mode) (Hz)	data rate Ch 2 (non coinc. mode) (Hz)	file name (coinc. mode)	data rate (coinc. mode) (Hz)	date (gg/mm/aaaa)	C (mm)	h (mm)	z_s (mm)	grid frequency f (Hz)	relative level (mm)	duration (s)	comments
run_80	NA	NA	NA	NA	NA	NA	NA	NA	NA	NA	NA	only NIDAQ file for still water level
run_81	NA	NA	run_81_bis	NA	22/04/2010	100	660	252	3.3	-3	NA	probe angle θ = 45° DAT file not available for new elaboration
run_82	NA	NA	run_82_bis	NA	22/04/2010	100	660	252	3.3	-4	NA	probe angle θ = 45° DAT file not available for new elaboration
run_83	940	440	run_83_bis	83	22/04/2010	100	660	252	3.3	-5	271	probe angle θ = 45°, β = 2.6° (upward)
run_84	980	445	run_84_bis	84	22/04/2010	100	660	252	3.3	-6	250	probe angle θ = 45°, β = 2.6° (upward)
run_85	991	447	run_85_bis	85	22/04/2010	100	660	252	3.3	-7	253	probe angle θ = 45°, β = 2.6° (upward)
run_86	1017	453	run_86_bis	89	22/04/2010	100	660	252	3.3	-8	251	probe angle θ = 45°, β = 2.6° (upward)
run_87	1020	450	run_87_bis	87	22/04/2010	100	660	252	3.3	-9	251	probe angle θ = 45°, β = 2.6° (upward)
run_88	998	444	run_88_bis	85	22/04/2010	100	660	252	3.3	-10	249	probe angle θ = 45°, β = 2.6° (upward)
run_89	975	429	run_89_bis	80	22/04/2010	100	660	252	3.3	-12	252	probe angle θ = 45°, β = 2.6° (upward)
run_90	946	398	run_90_bis	73	22/04/2010	100	660	252	3.3	-15	250	probe angle θ = 45°, β = 2.6° (upward)
run_91	891	351	run_91_bis	64	22/04/2010	100	660	252	3.3	-20	249	probe angle θ = 45°, β = 2.6° (upward)
run_92	699	330	run_92_bis	51	22/04/2010	100	660	252	3.3	-25	249	probe angle θ = 45°, β = 2.6° (upward)
run_93	859	341	run_93_bis	59	22/04/2010	100	660	252	3.3	-30	247	probe angle θ = 45°, β = 2.6° (upward)
run_94	886	369	run_94_bis	61	22/04/2010	100	660	252	3.3	-40	258	probe angle θ = 45°, β = 2.6° (upward)
run_95	849	351	run_95_bis	55	22/04/2010	100	660	252	3.3	-50	262	probe angle θ = 45°, β = 2.6° (upward)
run_96	840	313	run_96_bis	61	22/04/2010	100	660	252	3.3	-5	256	probe angle θ = 135°, β = 2.6° (upward)
run_97	870	321	run_97_bis	50	22/04/2010	100	660	252	3.3	-10	248	probe angle θ = 90°, β = 2.6° (upward)

run_98	850	352	run_98_bis	65	22/04/2010	100	660	252	3.3	-10	251	probe angle θ = 135°, β = 2.6° (upward)
run_99	699	326	run_99_bis	46	22/04/2010	100	660	252	3.3	-10	247	probe angle θ = 0°, β = 2.6° (upward)
run_100	769	334	run_100_bis	64	22/04/2010	100	660	252	3.3	-10	251	probe angle θ = 45°, β = 2.6° (upward)

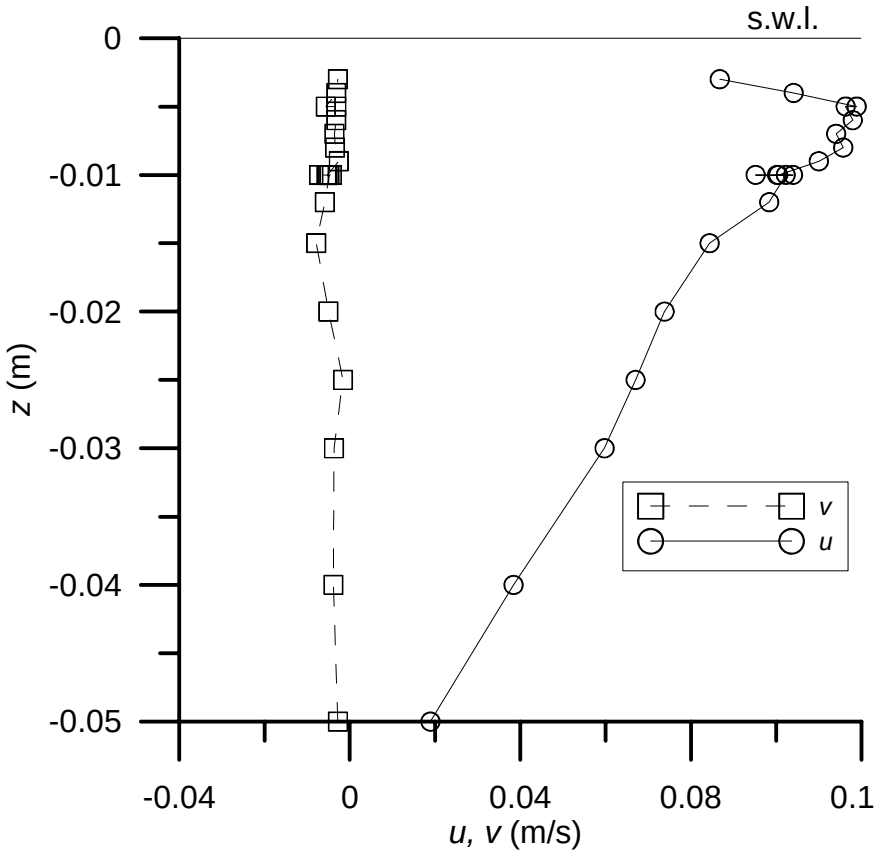

Figure A.7. Mean horizontal (*u*) and vertical (*v*) velocity profile

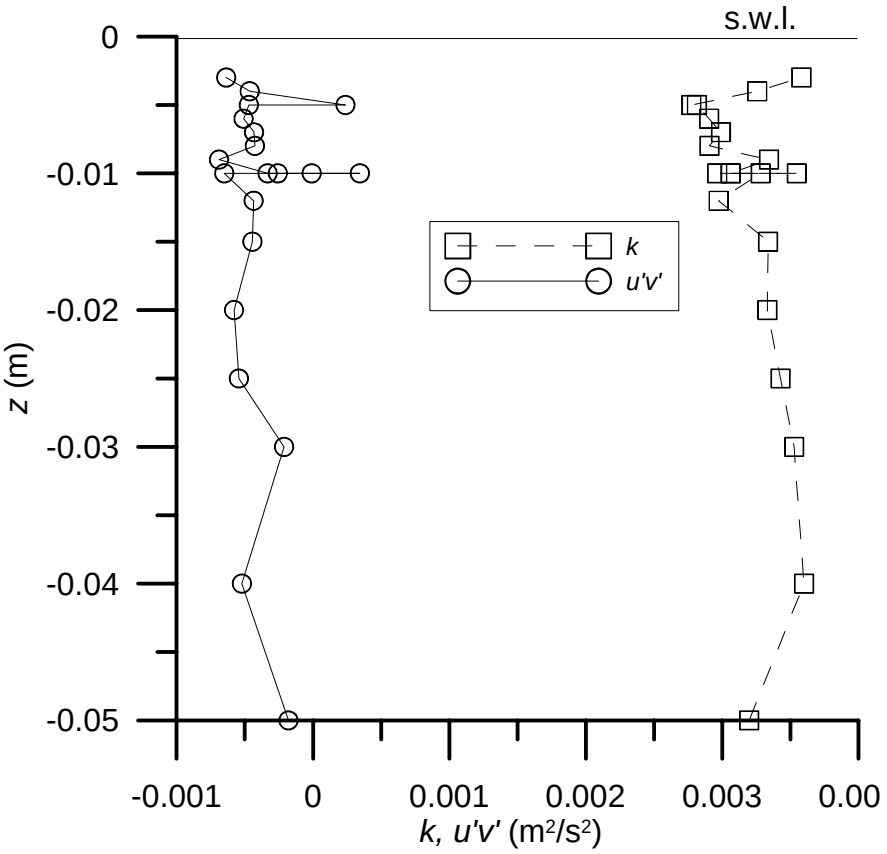

Figure A.8. Turbulent kinetic energy (*k*) and Reynolds tangential stress (*u'v'*) profile.

Table A.8. Water velocity measurements. x = -50 mm. Stroke ±50 mm

file name (non coinc. mode)	data rate Ch 1 (non coinc. mode) (Hz)	data rate Ch 2 (non coinc. mode) (Hz)	file name (coinc. mode)	data rate (coinc. mode) (Hz)	date (gg/mm/aaaa)	C (mm)	h (mm)	z_s (mm)	grid frequency f (Hz)	relative level (mm)	duration (s)	comments
run_101	78	86	run_101_bis	1	23/04/2010	100	660	252	3.3	2	258	probe angle θ = 0°, β = 8.0° (upward)
run_102	459	520	run_102_bis	20	23/04/2010	100	660	252	3.3	1	261	probe angle θ = 0°, β = 8.0° (upward)
run_103	665	570	run_103_bis	17	23/04/2010	100	660	252	3.3	0	258	probe angle θ = 0°, β = 8.0° (upward)
run_104	680	438	run_104_bis	10	23/04/2010	100	660	252	3.3	-1	253	probe angle θ = 0°, β = 8.0° (upward)
run_105	745	429	run_105_bis	11	23/04/2010	100	660	252	3.3	-2	250	probe angle θ = 0°, β = 8.0° (upward)
run_106	774	429	run_106_bis	11	23/04/2010	100	660	252	3.3	-3	250	probe angle θ = 0°, β = 8.0° (upward)
run_107	647	405	run_107_bis	8	23/04/2010	100	660	252	3.3	-4	251	probe angle θ = 0°, β = 8.0° (upward)
run_108	727	384	run_108_bis	9	23/04/2010	100	660	252	3.3	-5	251	probe angle θ = 0°, β = 8.0° (upward)
run_109	691	359	run_109_bis	8	23/04/2010	100	660	252	3.3	-6	252	probe angle θ = 0°, β = 8.0° (upward)
run_110	742	338	run_110_bis	9	23/04/2010	100	660	252	3.3	-7	251	probe angle θ = 0°, β = 8.0° (upward)
run_111	694	322	run_111_bis	8	23/04/2010	100	660	252	3.3	-8	252	probe angle θ = 0°, β = 8.0° (upward)
run_112	699	314	run_112_bis	8	23/04/2010	100	660	252	3.3	-9	250	probe angle θ = 0°, β = 8.0° (upward)
run_113	677	302	run_113_bis	7	23/04/2010	100	660	252	3.3	-10	251	probe angle θ = 0°, β = 8.0° (upward)
run_114	683	323	run_114_bis	8	23/04/2010	100	660	252	3.3	-15	251	probe angle θ = 0°, β = 8.0° (upward)
run_115	636	344	run_115_bis	7	23/04/2010	100	660	252	3.3	-20	266	probe angle θ = 0°, β = 8.0° (upward)
run_116	555	500	run_116_bis	16	23/04/2010	100	660	252	3.3	1	250	probe angle θ = 0°, β = 8.0° (upward)
run_117	572	471	run_117_bis	12	23/04/2010	100	660	252	3.3	0.5	251	probe angle θ = 0°, β = 8.0° (upward)
run_118	398	411	run_118_bis	14	23/04/2010	100	660	252	3.3	1.5	253	probe angle θ = 0°, β = 8.0° (upward)
run_119	91	105	run_119_bis	2	23/04/2010	100	660	252	3.3	2	285	probe angle θ = 0°, β = 8.0° (upward)

run_120	29	26	run_120_bis	0	23/04/2010	100	660	252	3.3	2.5	NA	probe angle θ = 0°, β = 8.0° (upward) coincident data NA

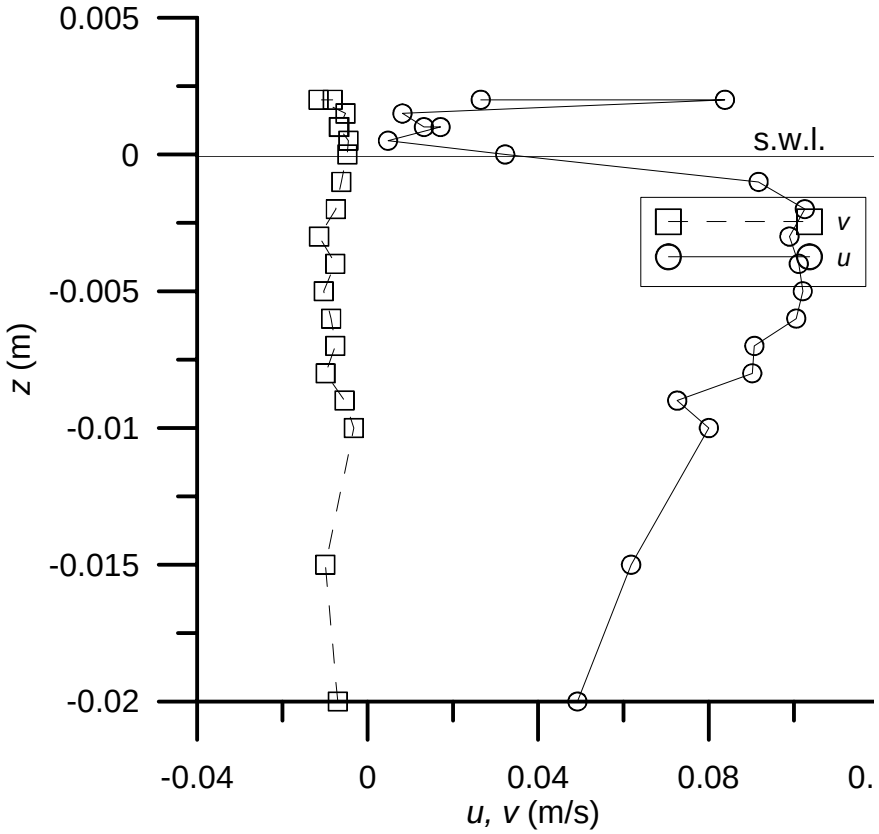

Figure A.9. Mean horizontal (*u*) and vertical (*v*) velocity profile

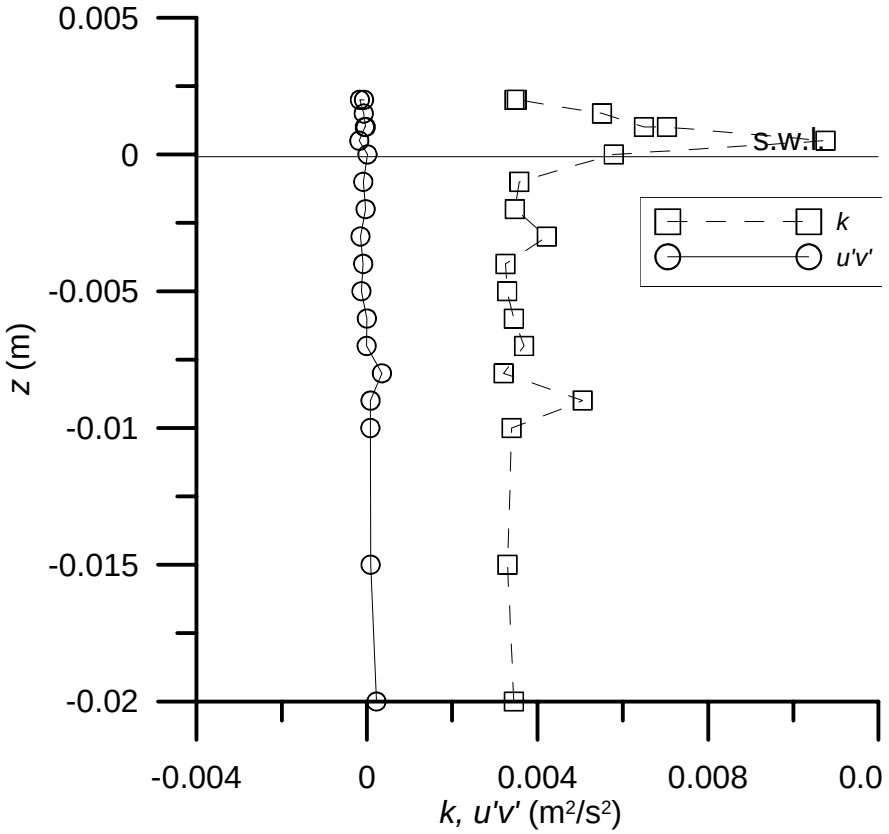

Figure A.10. Turbulent kinetic energy (*k*) and Reynolds tangential stress (*u'v'*) profile.

Appendix B

PROCEDURE OF PROBE ALLIGNMENT

THE PROCEDURE IS NECESSARY IF THE LASER BEAMS COMING OUT FROM THE PROBE DO NOT CROSS ADEQUATELY AND/OR THE RECEIVING FIBRE IS NOT ALIGNED WITH THE BEAM CROSSING

In order to achieve a good data rate and a good quality of the measurements, three requirements must be satisfied:

- the light beams have to cross properly to define the *measurement volume*;
- the receiving fibre has to be aligned with the beam crossing;
- the focus plane of the receiving fibre has to intersect the beam crossing so that the *viewing volume* coincides with the measurement volume.

These three conditions ensure that the measurement volume is the maximum available (total overlap of the beams) and that the receiving fibre is properly oriented to detect the light reflected by scatters moving through the measurement volume.

Before proceeding with the measurements, the following steps should be performed:

- checking beam crossing – for each beam couple AND for the four beams together;
- verifying the alignment of the receiving fibre with the beam crossing.

1. CHECK BEAM CROSSING

Material: probe, microscope, clamping device (to fix the probe and the microscope)

NB: power << 300 mW

1.1. Prepare a stable support (a board or firm surface) to which the microscope and the probe can be clamped; consider that the beam footprints have to be projected on a wall or surface at least 1 m away from the position of the microscope.

1.2. Position the probe on the support and clamp it or bolt it to the support.

1.3. Position the microscope on the support: the microscope must be located in a position such that the four beams coming out from the probe cross at the front lens of the microscope objective. This way the position of the microscope coincides with the location of the measurement volume (hence, the distance between the lens of the probe and the lens of the microscope should be almost equal to the focal length of the

transmitting lens). This is very important for the success of the procedure; be careful because the projection of the beams is very sensible to the location and orientation of the microscope objective. The beams enlarged by the microscope have to be aligned with the probe (a small angle between the optic plane of the microscope and the plane orthogonal to the incident beams generate a strong deflection of the enlarged beams). Note that the tiny control of the microscope position is obtained screwing the optic of the microscope.

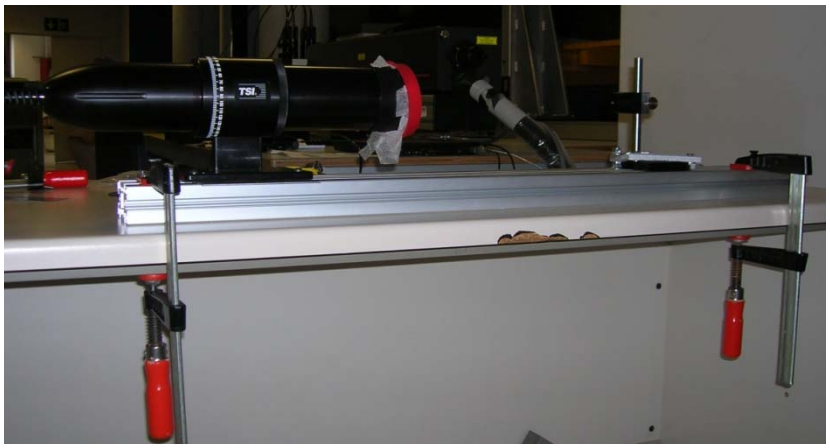

Layout of the probe and microscope on a board clamped to the table

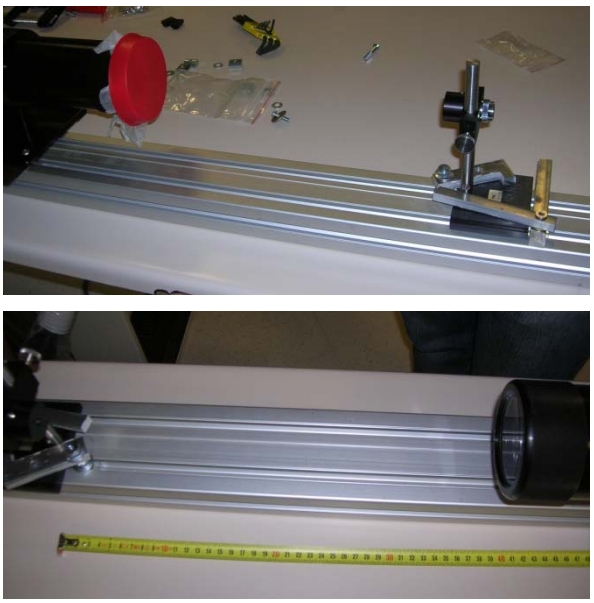

Layout of the probe and microscope over the board (each one is clamped in position) and distance between the probe and microscope objective.

1.4. Check beam crossing:

1.4.1. Verify each beam couple separately. Start with the GREEN beams:

1.4.1.1. Close the shutters of the blue light couplers and concentrate on the GREEN beams.

1.4.1.2. Move the objective of the microscope towards and away from the probe (back and forth); as the objective moves around the crossing point you should see the footprints of the beams departing and then intersecting, as the objective respectively goes away from or approaches the crossing point

1.4.1.3. When the microscope objective is at the crossing point, the footprints of the two beams should overlap by at least the 80% of their diameter. If this is not the case, beam steering is needed.

1.4.1.4. Close the shutters of the green light couplers.

1.4.2. Check the crossing of the BLUE beams repeating steps (1.4.1.1-1.4.1.3).

1.4.3. Verify the crossing of all four beams: the two sets of beams should overlap by at least 80% of the diameter. This requirement is less critical, but still important.

2. CHECK THE ALIGNMENT OF THE RECEIVING FIBRE

Material: probe, microscope, clamping device (to fix the probe and the microscope), backlight adaptor or alignment check cable (1098416).

NB: power << 300 mW

2.1. Set up the working space

2.1.1. Prepare a stable support on which the microscope and the probe can be clamped; consider that the beam footprints have to be projected on a wall or surface at least 1 m away from the position of the microscope.

2.1.2. Position the probe on the support and clamp it to the support.

2.1.3. Set the rotational position of the probe to 0 deg and tighten the locking wheel.

2.1.4. Position the microscope on the support: the microscope must be located in a position such that the four beams coming out from the probe cross at the

front lens of the microscope objective. This way, the position of the microscope coincides with the location of the measurement volume (hence, the distance between the lens of the probe and the lens of the microscope should be almost equal to the focal length of the transmitting lens). Do not lock the microscope tightly since it will likely be moved from this position if the viewing volume does not coincide with the beam crossing position.

2.1.5. Fix the cable conveying the fibreoptics in and out of the probe to the support.

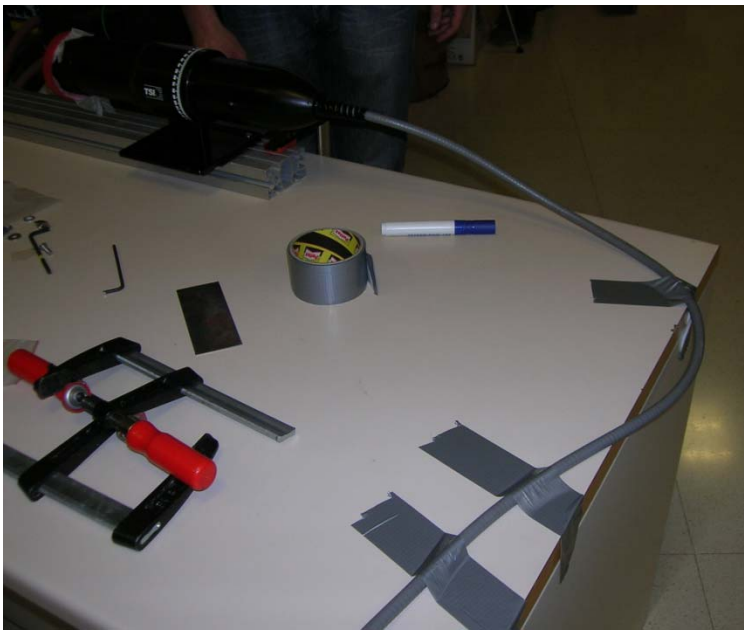

Fastening of the cable to the table.

2.2. Determine the viewing volume of the receiving fibre:

2.2.1. Close the beam shutter of the GREEN SHIFTED transmitting fibre and disconnect it the from the coupler

2.2.2. Disconnect the receiving fibre from the photodetector PDM

2.2.3. Take the alignment check cable and place the end with the TSI connector inside the green shifted coupler

(a) Alignment check cable and (b) TSI connector of the check alignment cable inside the green shifted shutter.

2.2.4. Hold the opposite end of the cable (where the SMA connector is) and point it towards a non-reflective surface about 10 cm away and adjust the focus and the upper knobs of the coupler to maximize the light emitted by the SMA end of the cable. Close the shutter

2.2.5. Take the receiving fibre and remove the adaptor from the SMA end (the piece that was going inside the PDM) – this will expose the fibre

Removal of the connector at the end of the receiving fibre.

2.2.6. Connect the SMA end of the receiving fibre with the SMA connector of the check alignment cable

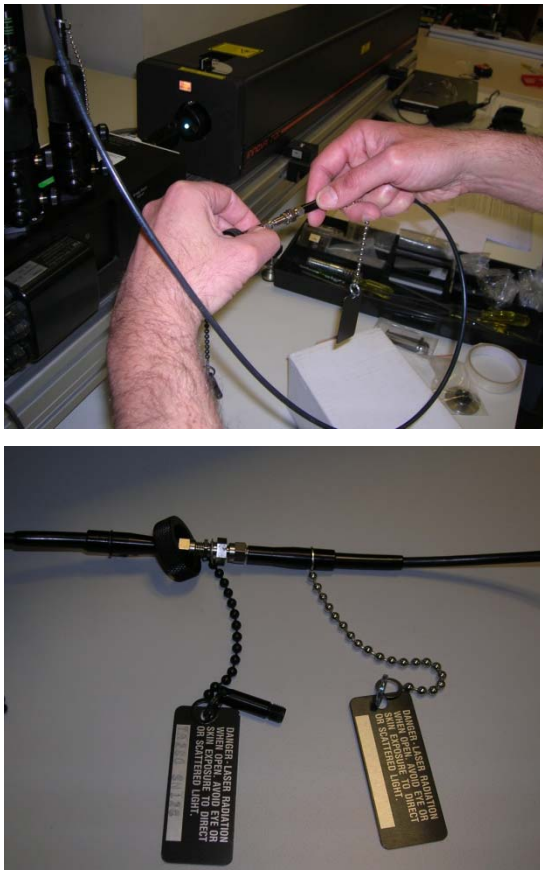

Connection of the receiving fibre to the check alignment cable.

2.2.7. Open the green shifted shutter: a speckled spot of green light should be projected by the probe on the wall or surface

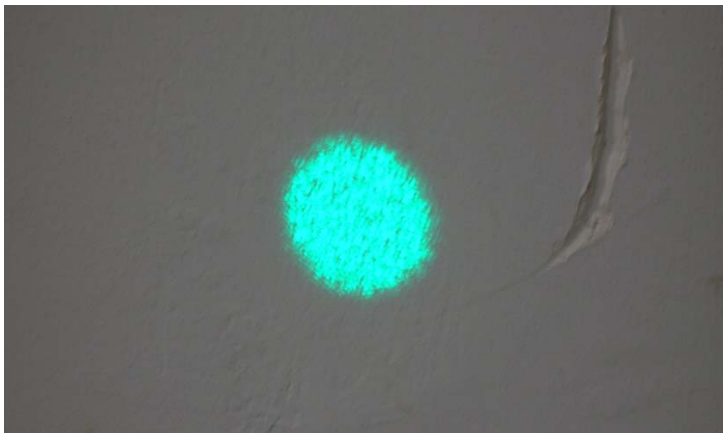

Projection of the receiving beam.

2.2.8. Slowly move the microscope objective towards and away from the probe and observe the spot of green light. Its diameter and the quality of the edge change based on the position of the microscope. Lock the microscope in the

position that minimizes the diameter of the spot while making the edge of the circle the sharpest possible. This is the position of the viewing volume. The microscope should not move from this position for the whole duration of the operations that follow.

2.2.9. Open the GREEN UNSHIFTED and BOTH BLUE shutters (if necessary, reduce the green light intensity reducing the power input at minimum, 10.1 A current mode for the laser, reducing the power by tilting the back mirror of the laser; green light decays faster than blue light): ideally the footprints of the three beams should be perfectly overlapped and the spot of the receiving fibre should be centered on the beam crossing. The loss of signal is proportional to how much the receiving and the transmitting spots do not overlap.

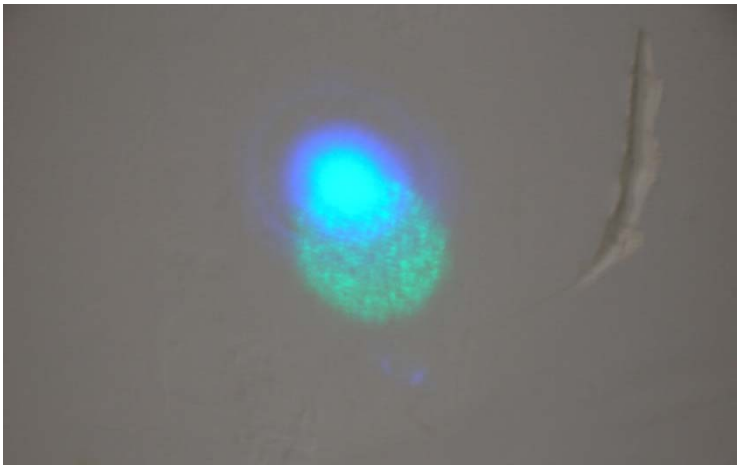

Example of misalignment between the beam crossing (blue) and the receiving fibre (green)

3. CORRECTION OF THE BEAM CROSSING AND ALIGNMENT WITH THE RECEIVING FIBRE

Material: probe, microscope, clamping device (to fix the probe and the microscope), backlight adaptor or alignment check cable (1098416), 0.050'' ball drivers and 0.035'' L-key (we used a 0.025'' ball driver).

3.1. The initial set-up is the same used to check the alignment of the receiving fibre.

3.2. Close the shutters of the couplers and of the fibrelight box.

3.3. Unscrew the secure screws of the tailpiece cover and **carefully remove** the cover of the tailpiece of the probe, exposing the fibres. Avoid rocking, tilting or kinking. Don't pull the fibres. Attach the tailpiece to the table using strong tape.

Layout of the tailpiece and of the probe

The central fibre is the receiving fibre and the four fibres around it are the transmitting fibres; each of the transmitting fibres is connected to a cylindrical wedge which is locked in its position by four screws. On the wedge are two grooves (holes), which are used to steer the beams; each of the grooves is locked by two of the screws.

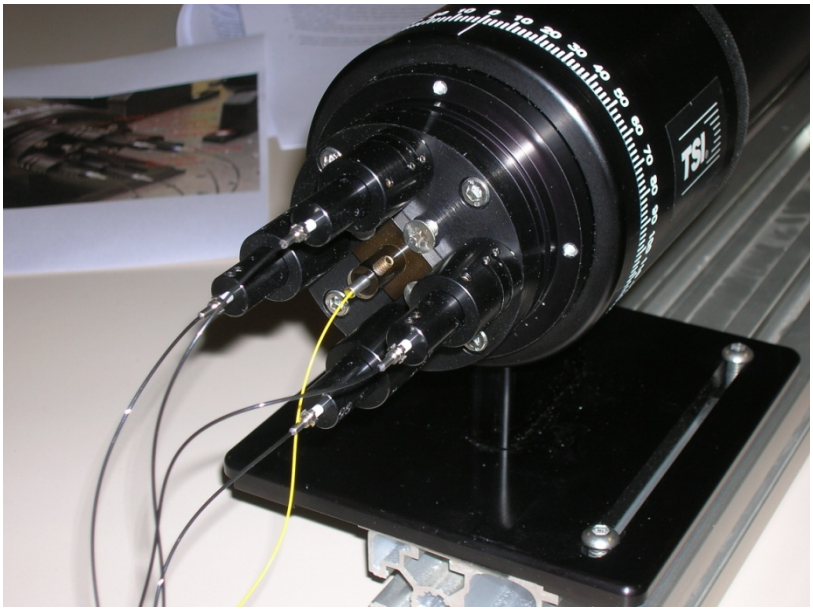

Fibres and wedges

3.4. Open the shutter of the fibrelight box and of each coupler (one at the time) to check which of the transmitting beams needs steering. If more than one does, start from the BLUE ones.

3.5. Beam steering: select the beam which needs steering and proceed as follows

3.5.1. Close the coupler shutters; only the shutter of the receiving fibre and of the transmitting beam to be steered should be left open

3.5.2. Unlock the wedges by loosening the four screws using a 0.035'' L-key

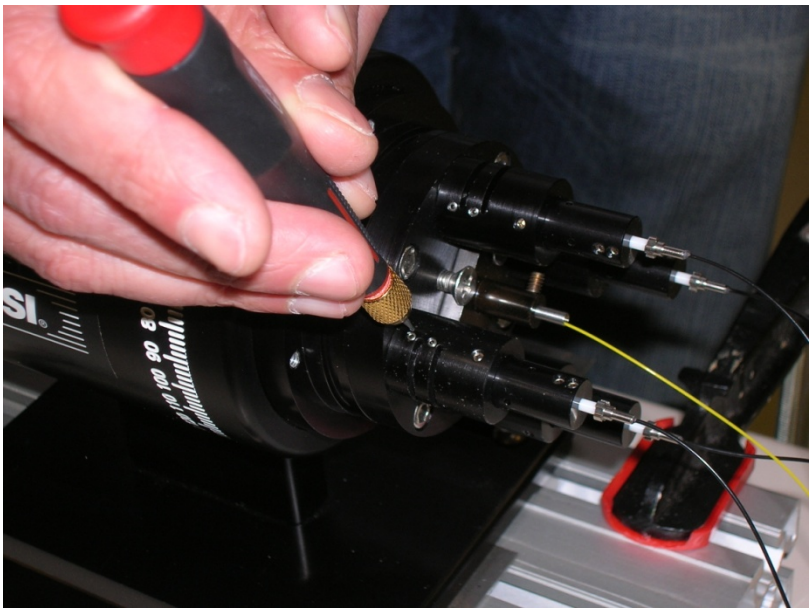

Unlocking the wedges

3.5.3. Steer the beam inserting a 0.050'' ball driver inside one of the holes of the groove and slightly moving the wedge. You can use two 0.050'' ball drivers, one for each groove, moving them at the same time. The position of the footprint is highly sensible to the movement of the wedge so move it slowly. The beam **moves in circles** not along a Cartesian reference system.

Steering the beam

3.5.4. Once the footprint of the beam is centered with respect to the spot of the receiving fibre, tighten the screws that lock the wedge of the fibre. This operation might induce unwanted displacements of the beam footprint – it might be necessary to repeat the steering several times until, after tightening, the final location of the footprint is correct. It happens most of the time.

3.6. Repeat the procedure for each fibre needing steering

3.7. Remove the receiving fibre from the coupler

3.7.1. Disconnect the receiving fibre from the check alignment cable

3.7.2. Reconnect the receiving fibre to the connector and insert it into the PDM

3.7.3. Remove the check alignment cable from the coupler

3.7.4. Insert the GREEN SHIFTED transmitting fibre into its coupler

3.8. Check the alignment of the GREEN SHIFTED beam with the other beams

3.9. If necessary, steer the green shifted beam until its footprint is overlapped with the crossing of the other three beams

3.10. Put the tailpiece of the probe back in place. **Proceed carefully**, avoiding rocking or pulling the fibres.